Region-specific modulation of somatostatin activity during arousal

Christine F. Khoury[1,2], Noelle G. Fala[2], Caroline A. Runyan*[1,2]

[1]Center for the Neural Basis of Cognition, [2]Department of Neuroscience, University of Pittsburgh

*Corresponding Author: Caroline A. Runyan, runyan@pitt.edu

Number of Pages: 34

Number of Figures: 6

Number of Tables: 6

Number of words for abstract: 250

Number of words for introduction: 640

Number of words for discussion: 1174

Conflict of Interest Statement: The authors declare no competing financial interests.

Acknowledgments: We thank Chengcheng Huang, Ross Williamson, and members of the Runyan lab for comments on the manuscript. This research was supported in part by the University of Pittsburgh Center for Research Computing through the resources provided. Judith Joyce Balcita-Pedicino performed histology and immunohistochemistry. We thank the GENIE project (Janelia) for making GCaMP sensors available for use. We thank the developers of Suite2P and Wavesurfer. This work was supported by the Andrew W. Mellon Predoctoral Fellowship, NIH Predoctoral Training Grant in Basic Neuroscience (T32 NS007433-21), Pew Biomedical Scholars Program, the Searle Scholars Program, the Klingenstein-Simons Fellowship Award in Neuroscience, and NIH grants NIMH DP2MH122404, NINDS R01NS121913.

Abstract

Arousal powerfully and globally influences cortical activity, yet the local circuits implementing these effects are poorly understood, especially outside of sensory cortex. Somatostatin-expressing inhibitory interneurons (SOM) densely innervate local populations, and their activity is highly sensitive to changes in brain state. SOM neurons are thus well-situated to modulate local population activity in response to shifts in arousal, yet the relationship between arousal state and SOM activity has not been characterized outside of sensory cortex. To compare the modulation of SOM neurons in sensory and association cortex across behavioral states, we imaged spike-related responses in SOM and Non-SOM neurons in auditory cortex (AC) and posterior parietal cortex (PPC) in mice of both sexes during spontaneous shifts in arousal state, using two-photon calcium imaging. The relationship between neuronal activity and arousal depended on both cell type and brain area. In PPC, neurons were positively modulated during periods of increased arousal, while the effects of arousal in AC neurons were more diverse. In PPC, the effects of arousal were strongest in the SOM population, while in AC SOM and Non-SOM populations were similarly modulated during shifts in arousal. Although arousal and overall activity were more strongly correlated in PPC, the readout of sensory information from population activity was enhanced during periods of high arousal in AC, but not PPC. Our findings suggest unique relationships between activity in local inhibitory subnetworks and arousal across cortex, which may be tailored to the roles of specific cortical regions in sensory processing or the control of behavior.

Significance statement: The effects of arousal on brain networks are profound but vary across regions. Somatostatin neurons may carry out some of the effects of arousal on local network activity in sensory cortex, by modulating response gain and decorrelating population activity. Yet it is unknown whether SOM neurons are similarly affected by shifts in brain state in association cortex, where they have not been well studied. Here, we have revealed differences in the effects of behavioral correlates of arousal on SOM neurons in auditory and parietal cortex, suggesting that specializations in SOM subnetworks could contribute to the diversity of arousal-related activity across cortical regions.

Introduction

Arousal and its associated behavioral states globally modulate brain activity (Livingstone and Hubel, 1981; Marrocco et al., 1994; Cantero et al., 1999; Gould et al., 2011; Grent-'t-Jong et al., 2011), but the relationship between aroused states and neuronal population activity has been most thoroughly explored in sensory cortex. In rodent sensory cortices, the effects of arousal are analogous to those of attention in the primate visual system (Treue and Maunsell, 1996; McAdams and Maunsell, 1999; Cohen and Maunsell, 2009; Mitchell et al., 2009; Rabinowitz et al., 2015), and include decorrelation of local population activity (Poulet and Petersen, 2008; Zhou et al., 2014; Vinck et al., 2015; Lin et al., 2019), enhanced response gain (Niell and Stryker, 2010; Polack et al., 2013; Fu et al., 2014; McGinley et al., 2015; Mineault et al., 2016) and an improved signal:noise ratio (Bennett et al., 2013; Polack et al., 2013; Vinck et al., 2015). However, even across sensory cortices, the effects of arousal on neuronal activity are not uniform (Shimaoka et al., 2018). For example, in auditory cortex (AC), but not other modalities, the effects of arousal are complicated by negative motor-related feedback from motor cortex through local inhibitory interneurons (Schneider et al., 2014; Zhou et al., 2014; Yavorska and Wehr, 2021). Despite these differences, aroused behavioral states are associated with improved stimulus coding in sensory cortices across modalities (Pinto et al., 2013; Chen et al., 2015; Lin et al., 2019). The circuits underlying these arousal-related effects are not fully understood, though inhibitory interneurons are likely to play important roles in controlling state-dependent shifts in population coding.

The inhibitory cell class can be divided into three nonoverlapping subtypes, which express parvalbumin (PV), somatostatin (SOM), or vasoactive intestinal peptide (VIP), and exhibit distinct local connectivity patterns (Tremblay et al., 2016). Transitions to aroused states, marked by widespread release of neuromodulators such as norepinephrine or acetylcholine, profoundly impact the activity of inhibitory interneurons (Alitto and Dan, 2013; Chen et al., 2015; Garcia-Junco-Clemente et al., 2019). SOM neurons are particularly sensitive to arousal state fluctuations, through direct activation of cholinergic and noradrenergic receptors (Kawaguchi and Shindou, 1998; Xiang et al., 1998; Beierlein et al., 2000;

Fanselow et al., 2008; Chen et al., 2015; Kuchibhotla et al., 2016), and through inhibition by VIP neurons (Pfeffer et al., 2013; Pi et al., 2013; Fu et al., 2014; Karnani et al., 2016; Garcia-Junco-Clemente et al., 2017; Dipoppa et al., 2018). In turn, SOM neurons can powerfully influence local network activity, as they densely innervate the local excitatory population (Fino and Yuste, 2011; Pfeffer et al., 2013; Xu et al., 2013). SOM neurons enhance stimulus selectivity and response reliability (Adesnik et al., 2012; Wilson et al., 2012; Rikhye et al., 2021), control local population activity dynamics (Chen et al., 2015; Veit et al., 2017), and flexibly modulate excitatory responses to stimuli based on behavioral relevance (Kato et al., 2015; Wang and Yang, 2018).

The density of SOM neurons is increased relative to PV neurons in association cortex (Kim et al., 2017; Dienel et al., 2020), suggesting that population level computations that SOM neurons participate in may differ across the cortical hierarchy. However, the functional properties of SOM neurons outside of sensory cortex remain largely uncharacterized. Here, we examined the relationship between neuronal activity in sensory (auditory cortex, AC) and association cortex (posterior parietal cortex, PPC) and the arousal state of spontaneously behaving mice, revealing clear area-specific differences. Neuronal activity in PPC, especially in SOM neurons, was strongly and positively modulated by behavioral correlates of arousal. In AC, neuronal activity was only weakly related to arousal state and included both positively and negatively modulated neurons. Our results suggest specialization in the relationship between brain state and population activity across the cortical hierarchy. Such specialization may be tailored to region-specific roles, i.e., auditory perception in AC and multimodal integration and navigation in PPC.

Materials and Methods

1.0 Experimental Design and Statistical Analysis

All pairwise comparisons were done with two-sided paired or unpaired permutation (i.e. randomization) tests with 10,000 iterations as indicated, where $p<0.0001$ indicates the highest significance achievable given the number of iterations performed. Given that the exact p value is unknown in these cases, p values of the highest significance are reported as such rather than as an exact value. All permutation tests were performed for differences in means. For statistical comparisons involving more than two groups, we used Kruskal-Wallis (non-parametric ANOVA) and used unpaired permutation tests post-hoc to determine which groups differed from each other. Data fell into natural groupings by 1) brain area (AC or PPC) and by 2) cell-type (SOM or Non-SOM), as indicated by expression of the red fluorophore, tdTomato. All bar plots show mean and bootstrapped 95% confidence intervals using 1000 iterations unless otherwise indicated. When multiple comparisons were made between groups, significance thresholds were Bonferroni-corrected. Sample sizes were chosen based on previous studies comparing population activity dynamics across brain areas or cell types (Runyan et al., 2017; Khan et al., 2018).

2.0 Animals

All procedures were approved by the University of Pittsburgh Institutional Animal Care and Use Committee. Homozygous SOM-Cre mice (Sst-IRES-Cre, JAX Stock #013044) were crossed with homozygous Ai14 mice (RCL-tdT-D, JAX Stock #007914) obtained from Jackson Laboratory, ME, USA, and all experiments were performed in the F1 generation, which expressed tdTomato in SOM+ neurons. Mice were group housed in cages with between 2 and 4 mice. Adult (8-24 weeks) male and female mice were used for experiments (4 male, 2 female). Mice were housed on a reversed 12 hr light/dark cycle, and all experiments were performed in the dark (active) phase.

2.1 Surgical procedures

Mice were anesthetized with isoflurane (4% for induction, and 1-2% maintenance during surgery), and mounted on a stereotaxic frame (David Kopf Instruments, CA). Ophthalmic ointment was applied to cover the eyes (Henry Schein, NY). Dexamethasone was injected 12-24 hours prior to surgery, and carprofen and dexamethasone (Covetrus, ME) were injected subcutaneously immediately prior to surgery for pain management and to reduce the inflammatory response. Two 2 x 2 mm craniotomies were made over left AC (centered at 3.0 mm posterior and 4.3 mm lateral to bregma) and PPC (centered at 2 mm posterior and 1.75 mm lateral to bregma). 1-4 evenly spaced ~60 nl injections of the AAV1-synapsin-l-GCamp6f (Addgene, MA stock #100837) that had been diluted to a titer of ~1x10^12 vg/mL using sterile PBS were made in each cranial window, centered on the same coordinates listed above. A micromanipulator (QUAD, Sutter, CA) was used to target injections ~250 µm under the dura at each site, where ~60 nl virus was pressure-injected over 5-10 minutes. Pipettes were not removed until 5 minutes post-injection to prevent backflow. Dental cement (Parkell, NY) sealed a glass coverslip (3mm) over a drop of Kwik Sil (World Precision Instruments, FL) over the craniotomy. Using dental cement, a one-sided titanium headplate was attached to the right hemisphere of the skull. After mice had recovered from the anesthesia, they were returned to their home cages, and received oral carprofen tablets (Bio-Serv, NJ) for 3 days post-surgery.

3.0 Experimental Setup

3.1 Two-photon microscope

Images were acquired using a resonant scanning two-photon microscope (Ultima Investigator, Bruker, WI) at a 30 Hz frame rate and 512 x 512 pixel resolution through a 16x water immersion lens (Nikon CF175, 16X/0.8 NA, NY). On separate days, either AC or PPC was imaged at a depth between 150 and 300 µm, corresponding to layers 2/3 of cortex. For AC imaging, the objective was rotated 35-45 degrees from vertical, and for PPC imaging, it was rotated to 5-15 degrees from vertical, matching the angle of the cranial window implant. Fields of view were 500 μm^2 and contained 187±95 neurons, 20±10 (mean and

standard deviation) of which were classified as SOM . Excitation light was provided by a femtosecond infrared laser (Insight X3, Spectra-Physics, CA) tuned to 920 nm. Green and red wavelengths were separated through a 565 nm lowpass filter before passing through bandpass filters (Chroma, ET525/70 and ET595/50, VT). PrairieView software (v5.5, Bruker, WI) was used to control the microscope.

3.2 Behavioral monitoring

Running velocity was monitored on pitch and roll axes using two optical sensors (ADNS-98000, Tindie, CA) held adjacent to the spherical treadmill. A microcontroller (Teensy, 3.1, Adafruit, NY) communicated with the sensors, demixing their inputs to produce one output channel per rotational axis using custom code. Outputs controlling the galvanometers were synchronized with running velocity using a digital oscilloscope (Wavesurfer, Janelia, VA).

Pupil images were acquired at 1280 x 1024 pixels, at 10 Hz from an infrared (IR) camera focused on one eye (Flea3 FL3-U3-13Y3M-C ½" Monochrome USB 3.0 Camera, 1.0x SilverTL Telecentric Lens, FOV = 6.74mm X 5.39mm, Edmund Optics, NJ). The pupil was illuminated by the IR light emitted by the two-photon laser and required no additional IR illumination. Movies were acquired with Matlab Image Acquisition Toolbox (Mathworks, MA). Pupil area was determined in each pupil movie frame post-hoc using custom Matlab code (Mathworks, MA). The pupil was constricted by controlling ambient illumination with an array of LCD screens (LG LP097QX1, South Korea), to maintain a moderate pupil area baseline from which increases and decreases in area could be measured.

3.3 Experimental protocol

Imaging began 3-5 weeks post-surgery once robust expression of the GCaMP6f virus was observed. Imaging sessions lasted 60-90 min total, divided in half between spontaneous activity and passive listening (ordering was random), and alternated between AC and PPC across days. Fields of view were selected based on co-expression of viral GCaMP6f (all neurons) and transgenic tDTomato (SOM neurons). Multiple imaging sessions were performed in each cranial window, focusing at slightly different

depths and lateral/posterior locations within the imaging windows across sessions. AC and PPC were each imaged in six mice (biological replicates). Each cranial window was imaged up to 11 times (technical replicates). Imaging from a given cranial window was suspended when we observed nuclear inclusion in 2 or more cells in the field of view, which indicates an over-expression of GCaMP6f. In each imaging session, GCaMP6f fluorescence changes were imaged in SOM (tdTomato+) and Non-SOM neurons, while mice ran freely on a spherical treadmill. In the spontaneous context, no sensory stimuli were delivered, while in the passive listening context, location-varying sound stimuli were presented (see Methods section 3.4). Spontaneous and passive listening contexts lasted ~25-50 minutes each. The order in which the contexts occurred was random.

3.4 Sound stimuli

Either immediately before or following the spontaneous activity context phase of the imaging session, the same field of view was imaged for 25-50 minutes during passive listening. Four magnetic speakers were positioned in a semicircular array, centered on the mouse's head (MF1-S, Tucker-Davis, FL). The speakers were positioned at -90, -30,+30 and +90 degrees from the midline in azimuth and driven by Matlab through a digital/analog converter (National Instruments). Speakers were calibrated to deliver similar sound levels (~70 db) in a sound isolation chamber using a microphone at the same distance from the speakers as the mouse's head using a random incidence microphone (4939, Brüel & Kjær, Denmark). During passive listening, 1 or 2 second dynamic ripples (broadband stimuli created in Matlab by summing 32 tones spaced across 2-32 kHz, which fluctuated at 10-20 Hz (Elhilali et al., 2004) were presented from one of eight locations. Four of the sound locations corresponded to the locations of the four speakers (-90, -30, +30, +90 degrees), while the other four sound locations (-60, -15, +15, +60 degrees) were simulated using vector-based intensity panning, where the same sound stimulus was delivered to two neighboring speakers simultaneously, scaled by a gain factor (Runyan et al., 2017). Dynamic ripples were chosen to optimally drive populations of neurons in auditory cortex with diverse frequency tuning preferences. Each sound repeated three times at one location before switching to

another. Each ripple played from all eight locations in randomized order continuously throughout the session with a 240 ms gap between each sound. Output controlling the audio speakers recorded along with two-photon imaging galvo and running velocity using Wavesurfer (Janelia, VA), and these signals were aligned offline.

4.0 Data Processing

Imaging datasets from 24 AC fields of view and 20 PPC fields of view were included from 6 mice. We excluded any datasets with significant photobleaching or more than two filled cells (see above). We also excluded any AC or PPC dataset from analysis if fewer than 1/3 of neurons that were significantly responsive (according to our definition in section 5.1) to at least one sound location, as we were interested in the effect of arousal on both spontaneous and sound-evoked responses. For AC datasets, we analyzed single-cell responses to pure tones on a subset of fields of view from each mouse, and then anatomically aligned all fields of view from datasets collected from each window, to ensure each field of view lay in a region representing tone frequencies in the sonic range of the tonotopic axis of primary auditory cortex. We eliminated any datasets where >50% of tone-responsive neurons had a preferred frequency was in the ultrasonic range (>20kHz), as well as any fields of view that were aligned anterior to a field of view where this was observed, to assure that we were seeing sound responses in the range of frequencies primarily represented by our dynamic ripples (described in section 3.4). We collected widefield fluorescence responses to pure tones in all AC cranial windows and observed ample pure tone responses in the sonic range for all AC windows; however, the extent of the viral expression within windows was too spatially limited to allow for mapping of specific regions.

4.1 Image Processing

For each field of view, the raw calcium movies collected during the spontaneous activity and passive listening contexts were concatenated prior to motion correction, cell body identification, and fluorescence and neuropil extraction. These processing steps were performed using Suite2p 0.9.3 in Python (Pachitariu

et al., 2017). Suite2p first registered images to eliminate brain motion, and clustered neighboring pixels with similar time courses into regions of interest (ROIs). ROIs were manually curated using the Suite2p GUI, to ensure that only cell bodies as opposed to dendritic processes were included in analysis, based on morphology. Cells expressing tdTomato (SOM cells), were identified using a threshold applied in the Suite2p GUI based on mean fluorescence in the red channel after bleed-through correction applied by Suite2p's cell detection algorithm, along with manual correction. For each ROI, Suite2p returned a raw fluorescence timeseries, as well as an estimate of neuropil fluorescence that could contaminate the signal. For each cell, we scaled the neuropil fluorescence by a factor by 0.7 and subtracted this timeseries from the ROI's raw fluorescence timeseries to obtain a neuropil-corrected fluorescence signal for each selected cell.

4.2 ΔF/F and deconvolution

Once the neuropil corrected fluorescence was obtained for each neuron, we calculated ΔF/F for each cell in each frame by calculating $(F-F_{baseline})/F_{baseline}$ for each frame, where F is the fluorescence of a given cell at that frame and $F_{baseline}$ was the eighth percentile of that cell spanning 450 frames before and after (~15s each way, 30 s total). ΔF/F timeseries were then deconvolved to estimate the relative spike rate in each imaging frame using the OASIS toolbox (Friedrich et al., 2017). We used the AR1 FOOPSI algorithm and allowed the toolbox to optimize the convolution kernel, baseline fluorescence, and noise distribution. A threshold of 0.05 a.u. was applied to remove all events with low magnitude from deconvolved activity timeseries. All analyses were performed with both ΔF/F and deconvolved activity, and showed the same trends. Outside of Figure 1F and 1H only results using deconvolved activity are shown.

5.0 Single cell modulation by sound stimuli, running behavior, and pupil size

5.1 Sound responsiveness

Each neuron's deconvolved activity was first z-scored. Sound responsiveness was calculated based on the mean activity of each neuron aligned on sound onset. For each neuron, we calculated the difference

between the mean activity during the sound presentation at each location, and the mean activity in the 240 milliseconds prior to sound onset. We then compared the observed sound responsiveness of each neuron for each sound location to a shuffled distribution. Each cell's activity was shifted randomly by at least 5 seconds in time relative to sound location time series, and for 1000 time-shifted iterations, sound responsiveness to each sound location was recalculated. Each sound responsive neuron had a positive sound responsiveness value for at least one location that was greater than the 95th percentile of that cell's shuffled distribution for that location. All other neurons were not considered sound responsive.

5.2 Running bouts and modulation

Running bout onsets were defined as transitions in speed from below 10 cm/s to above 10 cm/s, and required that the mean running speed in the 1 s following the transition was three times greater than the 1 s prior to running bout onset, and that the mouse maintained a speed of a minimum of 15 cm/s for the following two seconds.

Running modulation was calculated as the difference in mean activity of a cell in the 1 s prior to running bout onset and the mean activity of a cell in the 3 s window following running bout onset. A shuffling procedure was applied to determine which cells were positively, negatively, and not modulated by running. Each cell's activity was shifted randomly by at least 5 seconds in time relative to running speed timeseries, and for 1000 time-shifted iterations, running modulation was recalculated. Positively modulated neurons had positive running modulation values higher than the 97.5th percentile of that cell's shuffled distribution. Negatively modulated cells had negative running modulation values lower than the 2.5th percentile of that cell's shuffled distribution. All other cells were considered to be not modulated by running speed increases.

5.3 Pupil dilation events and modulation

Pupil area was normalized to its maximum across the imaging session. To identify pupil dilation events, we first identified all local maxima of the pupil area. We then found the point prior to this where the

derivative of pupil area was zero. We included events where the change from the inflection point to the local maximum was at least a 40% increase in pupil area and that the change from inflection point to local maximum was less than 1 second, and that the local maximum was at least 50% of the maximum total area by the pupil during that imaging session. We considered each inflection point to be the onset of dilation events.

To capture all pupil dilation related activity, which had a slower time course than running (Figure 2), we calculated pupil modulation for each neurons as the difference between the mean activity in the 1-s time window prior to dilation event onset and the mean activity in the 5-s time window following dilation event onset. We applied the same shuffling procedure as described for running modulation (5.2) to determine which neurons were positively, negatively, and not modulated by pupil dilation events.

6.0 Arousal States

6.1 Defining low and high arousal states based on pupil area

K-means clustering was applied to the full pupil area timeseries, which included both spontaneous activity and passive listening contexts, to classify each pupil area measurement as low, transitional, or high arousal. Each pupil area timeseries was mean normalized using the following equation:

$$\frac{x - \bar{x}}{\bar{x}}$$

The Manhattan (aka City Blocks) distance metric was applied to define 2 centroid clusters that served as the high and low arousal groups. Transition periods included timepoints when the absolute difference in distance to the high and low arousal centroids was less than 0.05.

6.2 Arousal Modulation Index

The arousal modulation index was calculated for each neuron using the following equation:

$$\frac{FR_{hi} - FR_{lo}}{FR_{hi} + FR_{lo}}$$

where FR_{hi} is the mean response of the neuron in the high arousal state and FR_{lo} is the mean response of the neuron in the low arousal state. We first maximum-normalized the deconvolved activity trace of each neuron across the entire time series. To calculate FR_{hi} (or FR_{lo}), we summed the activity from the high (or low) arousal state and divided by the total time spent in the high (or low) arousal state in the spontaneous (Figure 2) or passive listening (Figure 3) context. This index could vary continuously between -1 and +1, where negative values indicate higher activity in the low arousal state, and positive numbers indicate higher activity during the high arousal state.

7.0 Encoding Models

We used an encoding model to disentangle the contributions of pupil size and running speed to the activity of neurons in AC and PPC. In the Generalized Linear Model (GLM), the time-dependent effects of all measured external variables on each neuron's activity were estimated (Pillow et al., 2008; Runyan et al., 2017). Three classes of predictors were used in different combinations to quantify their contributions to neuronal activity: running, pupil size, and sound stimulus predictors. We used a Bernoulli-based GLM to weight various combinations of predictors based on these variables to predict each neuron's binarized activity (timeseries of relative spike rates were thresholded at 0.05). The encoding model is fully described in our previous work (Runyan et al., 2017).

7.1 Pupil size and running predictors

Running velocity was measured at a higher time resolution than imaging and was binned to match the sampling rate of two-photon images (30 Hz). We included the velocity along the pitch and roll axes of the treadmill (relative to the mouse's body axis). Running velocity measurements were separated into four channels, (1) forward, (2) reverse, (3) left, (4) right directions based on rotation along these axes. Running velocity changes could both precede or follow activity of individual neurons, so time series of running

velocity were convolved with four evenly spaced Gaussian basis functions (240 ms half-width at half-height) extending 1s both forward and backward in time (8 basis functions total for each running direction: forward, reverse, left, and right). Changes in pupil area were modeled similarly. Because pupil is a slower signal, the pupil area trace was convolved with 16 evenly spaced Gaussian basis functions 4 s forward and backward in time to allow for either prediction or response to pupil area changes.

7.2 Sound stimulus predictors

Sound stimuli were delivered from specific sound locations in the passive listening context. For sound stimulus onsets at each of the possible sound locations, 12 evenly spaced Gaussian basis functions (170 millisecond half width at half height) extended 2 s forward in time from each sound onset. First, second, and third repeats were represented separately due to potential adaptation-related effects. This resulted in 12 basis functions per repeat per sound location x 3 repeats x 8 locations for 288 sound predictors.

7.3 GLM fitting and cross-validation procedures

All predictors were maximum normalized before the fitting procedure. Beta coefficients for the predictors were fitted to each neuron's activity individually, using the glmnet package in R (Friedman et al., 2010) with elastic-net regularization, which smoothly interpolated between L_1 and L_2 type regularization according to the value of an interpolation parameter α, such that $\alpha=0$ corresponded to L_2 and $\alpha=1$ corresponded to L_1. We selected $\alpha=.25$.

Trials were randomly split into training (70% of trials) and testing (remaining 30% of trials) sets, while balancing the distribution of sound locations. Fitting was performed on the training set, and within each training dataset, cross-validation folds (3x) were also pre-selected so that sound locations were evenly represented. Model performance (see below, 7.4) was assessed on the test set. Each model was thus fitted and tested on entirely separate data to prevent over-fitting concerns. This train/test procedure was repeated ten times, with random subsamples of the data included in train and test segments. Each model's overall performance was assessed as its mean across all 10 iterations.

7.4 GLM model performance

Each model's performance for each cell was defined as the fraction of explained deviance of each model (compared to the null model). In the null model, only a constant (single parameter) was used to fit the neuron's activity and no time-varying predictors were included. First, we calculated the deviance of the null and behavior model variants (see Methods section 7.5). For each model, the fraction of null model deviance explained by the model (d) was then calculated ((null deviance – model deviance)/null deviance). Deviance calculations were performed on a test dataset (30% of the data), which had not been included in the fitting procedure, and this train/test procedure was repeated ten times on randomly subsampled segments of the data.

7.5 Running and pupil contribution

While running and pupil area fluctuations are highly correlated, they have separable influences on neuronal activity (Vinck et al., 2015). To identify the separate contributions of running and pupil area on SOM and Non-SOM neurons' activity, we fit three separate models: (1) full behavior model, (2) "no pupil" model, (3) "no running" model. In the full behavior model, all running, pupil, and sound predictors were included to fit each neuron's activity. The "no pupil" model did not include the pupil predictors, and the "no running model" did not include the running predictors.

We estimated the contribution of pupil or running to a neuron's activity that could not be compensated for by the other variables, by comparing the model performance (fraction deviance explained, see Methods section 7.4) in the full vs. no pupil or no running models,. The "running contribution" was calculated as the difference in fraction deviance explained of the full model and fraction deviance explained of the no-running model d_{fb}-d_{nr}. The "pupil contribution" was calculated as the difference in fraction deviance explained of the full model and fraction deviance explained of the no-pupil model d_{fb}-d_{np}.

8.0 Decoding

We used a population decoder to compare the sound location information contained in AC and PPC population activity, and its modulation with arousal state. The details of the decoder that we built to estimate the information about sound stimulus location have been previously described (Runyan et al., 2017). Briefly, for each trial we decoded sound stimulus location from single-trial population activity by computing the probability of external variables (sound location Left/Right category) given population activity. We used Bayes' theorem, relying on population response probabilities estimated through the full behavior GLM and its predictors in that trial, to compute the posterior probability of each possible sound location stimulus. The decoder was "cumulative" in time, as for each time point t, it was based on all imaging frames from the initiation of the trial through time t. The decoded stimulus location at each time t was defined as the stimulus location with the maximum posterior probability, based on individual neurons or on a population of simultaneously imaged neurons. The population could include SOM, Non-SOM, or the "best" neurons. Non-SOM neurons were randomly subsampled 10 times, matching the sample size of SOM neurons in each iteration. The "best" neurons were selected as the n individual neurons with the best decoding performance, where n is the number of SOM neurons simultaneously imaged. Decoder performance was calculated as the fraction of correctly classified trials at each time point.

To compare decoder performance in low and high arousal states, trials were classified as "low" or "high" arousal based on normalized pupil area (see section 7.2). Only the first sound repeat of each trial was used. Trials were randomly subsampled in the test set to ensure an even distribution of low and high arousal trials, and sound locations. This random subsample was repeated ten times.

9.0 Sound location selectivity

To assess the selectivity of sound-related activity in SOM and Non-SOM neurons in AC and PPC, trial-averaged responses were used to calculate the "location selectivity index", based on vector averaging in the preferred sound direction:

$$LSI = \sqrt{\left(\sum_{i=1}^{n} R(\Theta_i)cos(2\Theta_i)^{2} + \sum_{i=1}^{n} R(\Theta_i)sin(2\Theta_i)^{2}\right)} / \sum_{i=1}^{n} R_i$$

where R is the average response during the sound location presentation, and Θ is the sound location from -90 to +90 degrees, indexed by I = 1 to n (8). LSI can vary continuously from 0 (unselective) to 1 (selectively responding to only one sound location). Datasets that did not have a minimum of 20 trials for each of the eight sound locations were excluded.

10.0 Histology

After all imaging sessions had been acquired, each mouse was transcardially perfused with saline and then 4% paraformaldehyde. The brain was extracted, cryoprotected, embedded, frozen, and sliced. Once slide mounted, we stained brains with DAPI to be able to identify structure. We used anatomical structure to verify the locations of our injections in AC and PPC.

Results

To determine whether the effects of arousal on cell-type specific activity are conserved across sensory and association cortex, we compared spontaneous and sensory-evoked activity in auditory cortex (AC) and posterior parietal cortex (PPC) in six mice of both sexes. We used two-photon calcium imaging in superficial cortex to measure the spike-related activity of neurons positive and negative for the red fluorophore tdTomato, which was expressed transgenically in somatostatin-positive (SOM) neurons (Madisen et al., 2009; Taniguchi et al., 2011). We virally expressed the genetically encoded calcium indicator GCaMP6f in all layer 2/3 neurons of AC and PPC in each mouse (Chen et al., 2013). Mice were head-fixed and allowed to run voluntarily on a spherical treadmill. To track behavioral state, running velocity and pupil area were recorded throughout imaging sessions (Figure 1 A-B).

PPC SOM neurons were most strongly and positively modulated during behavioral state transitions

During each imaging session, we imaged AC or PPC in two contexts. During the "spontaneous" context, the mouse ran freely on the spherical treadmill in the absence of sensory stimulation. During "passive listening", sounds were presented from eight separate locations (Figure 1 B-C). We first examined how changes in pupil area and running speed corresponded with changes in activity of individual neurons during the spontaneous context. Throughout imaging sessions, mice spontaneously transitioned between behavioral states: stillness and running, and pupil constriction and dilation (Figure 1 F, H). To quantify the effect of behavioral state transitions on individual neurons' activity, we identified timepoints during the spontaneous context when either running speed or pupil area increased (Materials and Methods 5.2-5.3). The frequency of running bouts and dilation events was similar during PPC and AC imaging sessions ($p=0.59$ and $p=0.65$ respectively, permutation test, here and throughout unless otherwise noted, see Materials and Methods 1.0). Mice initiated running bouts at a rate of 0.915 [0.749, 1.11] (mean and [bootstrapped 95% confidence interval of the mean], here and throughout, unless otherwise indicated) bouts per minute, and pupil dilations at 0.981 [0.857, 1.12] dilations per minute. We observed no difference between AC (N=24) and PPC (N=20) imaging sessions when considering pupil area and

running speed during in passive listening or spontaneous contexts (passive running speed: p=0.20; spontaneous running speed: p=0.52; passive pupil area: p=0.43; spontaneous pupil area: p=0.73). Pupil area and running speed were higher during the passive listening context (pupil: 37.74% max. area [34.90%, 41.24%]; running: 26.50 cm/s [20.37, 36.77], N=44 datasets) relative to the spontaneous behavior context (pupil: 33.06% max. area [30.61%; 35.93%]; running 16.69 cm/s [13.81, 20.11], N=44 datasets) (pupil: p=0.0020, running: p<0.0001, paired permutation test, see Materials and Methods 1.0, N=44 datasets).

To determine how behavioral state affected neuronal activity, we first examined the activity of individual neurons during transitions from stationary to running. We compared mean activity of each neuron (deconvolved estimated spike rates, here and throughout) in the 3-s time window following running bout onset to the 1-s time window prior to running bout onset (Figure 1 I, See Materials and Methods 5.2). Pupil size modulation was calculated similarly, based on transitions in pupil area from constricted to dilated (Figure 1 D, J; Materials and Methods, 5.3). We compared each neuron's running and pupil modulation to shuffled distributions, where activity and behavioral data were time shifted by random intervals, and classified each neuron as positively, negatively, or not modulated by behavioral state transition. Larger proportions of the SOM and Non-SOM populations were positively modulated by both pupil dilations and running bout onsets in PPC than in AC (Figure 1 I-J), suggesting that the effects of arousal on spontaneous activity are not uniform across areas. Among the groups considered, the PPC SOM population had the greatest proportion of neurons modulated by running speed and pupil dilation (Figure 1 I-J).

Sound responsiveness of SOM and Non-SOM neurons' activity

Sound stimuli were presented from eight distinct locations, centered on the mouse's head (Figure 1 B-C, See Materials and Methods 3.4). We used these auditory stimuli due to PPC's role in spatial auditory processing during active behaviors (Nakamura, 1999; Runyan et al., 2017). To determine whether each

neuron was sound responsive, we computed the mean difference in activity during sound presentations and the pre-stimulus periods and compared to a shuffled distribution (Materials and Methods 5.1). Large proportions of neurons in both areas were significantly sound responsive, but a greater proportion of AC SOM and Non-SOM neurons were sound responsive compared to PPC (53% of AC SOM and 53% of AC Non-SOM relative to 44% of PPC SOM and 45% of PPC Non-SOM neurons, Figure 1 K).

SOM and Non-SOM neurons were differentially affected by behavioral state in PPC, but not AC

To further characterize the relationship between arousal state transitions and activity of single neurons in AC and PPC, we continued to focus on "running bouts", when the mouse's running speed rapidly increased, to define behavioral state transitions (Materials and Methods 5.2). The following analyses were based on the spontaneous context, when no sounds were played, to better isolate the effects of arousal changes from other variables driving neuronal activity. We aligned and averaged the pupil area measurements to running bout onsets, observing that pupil area also increased during running bouts, though with a slower time course (Figure 2 A, gray trace, N=44 imaging sessions). We also aligned and averaged the activity of SOM and Non-SOM populations from AC and PPC to running bout onset (Figure 2 A, colored traces, AC, N=24; PPC, N=20 imaging sessions from 6 mice). In both AC and PPC, mean activity of SOM and Non-SOM neurons increased with the onset of running bouts. However, this increase in activity was weak in AC, due to the prevalence of both positively and negatively modulated SOM and Non-SOM neurons in the AC population (Figure 2 B). Conversely, in PPC, Non-SOM and SOM neurons more uniformly increased activity at running onset (Figure 2 B).

Because of the slow time course of changes in pupil area compared to the more rapid transitions in locomotion (Figure 2 C-D), we also characterized single neuron activity during periods of sustained pupil constriction and dilation. We classified pupil measurements as corresponding to low, transitional, or high arousal states (Figure 2 E, Materials and Methods 6.1), and focused analyses on the low and high arousal states. As expected from the relationship between running speed and pupil area, running speed was higher

during the pupil-defined high arousal than low arousal states ($p<0.0001$). Mice ran on average 48.24±4.77 cm/s (mean±SEM) during the high arousal state, and 7.71±1.29 cm/s during the low arousal state ($p<0.0001$, N=44 datasets). SOM and Non-SOM activity was elevated overall in high arousal states ($p<0.0001$ for AC Non-SOM, PPC SOM and Non-SOM, $p=0.0029$ for AC SOM neurons, paired permutation test, Figure 2 E-H). To compare arousal modulation of activity in each population of neurons, we next computed an Arousal Modulation Index (AMI, Materials and Methods 6.2), which could vary from -1 to +1, with -1 indicating greater mean activity in the low arousal period, and +1 indicating greater activity in the high arousal period. The AMI was higher in PPC than AC neurons ($p<0.0001$, See Table 1 for full values and statistics). Interestingly, the AMI differed by cell type in PPC but not AC. In AC, the AMI was similar in SOM and Non-SOM neurons ($p=0.22$), while in PPC, the AMI was higher in SOM than Non-SOM neurons ($p<0.0001$, Figure 2 I).

Finally, to consider the full time-varying relationship between ongoing neuronal activity and behavioral correlates of arousal, we correlated each neuron's activity to pupil area and running speed, across the entire spontaneous behavioral context (Figure 2 J-K). Consistent with the above analyses based on activity aligned on state transitions, SOM and Non-SOM activity in PPC was more strongly correlated with both running and pupil size than in AC ($p<0.0001$). Within AC, SOM and Non-SOM activity was similarly correlated to the two behavioral measures (pupil area, $p=0.063$; running speed, $p=0.146$), while within PPC the activity of SOM neurons was again more strongly correlated with behavior than was the activity of Non-SOM neurons ($p<0.001$ for both running and pupil, Figure 2 J-K, See Table 2).

All analyses reported in Figure 2 relied on data collected during the spontaneous context to isolate the effects of arousal on spontaneous activity in the absence of sensory evoked responses. To determine whether arousal modulation differs during sensory stimulation, we repeated the analysis of the relationship between arousal correlates and activity in AC and PPC measured during the passive listening context (Figure 3). As in the spontaneous context, during passive listening both SOM and Non-SOM neurons in PPC had significantly higher arousal modulation index (AMI) values (Figure 3 E), as well as

correlation coefficients with running and pupil than AC ($p<0.0001$, Figure 3 F-G, See Table 3). Within AC, SOM and Non-SOM had similar AMI values ($p=.63$) and correlations with running speed ($p=.59$) and pupil area ($p=.63$). In contrast, within PPC, SOM neurons had significantly higher AMI values ($p<0.0001$) and correlations with running speed ($p<0.0001$) and pupil area ($p<0.0001$) than Non-SOM neurons. These results are consistent with what was observed in the spontaneous context, demonstrating that arousal modulation in AC and PPC is similar with and without sensory stimulation. See Tables 3 and 4 for a full summary of values and statistics for the passive listening context.

Taken together, our results so far indicate that SOM and Non-SOM neurons have heterogeneous activity relationships with arousal state in AC, whether defined by running speed or pupil area. In PPC, conversely, neuronal activity was positively modulated with heightened arousal. Furthermore, SOM neurons were differentially modulated in AC and PPC. In AC, no differences in arousal-modulation of SOM and Non-SOM neurons were evident; however, in PPC, SOM neurons were more sensitive to increases in arousal than Non-SOM neurons.

An encoding model to disentangle running speed and pupil size contributions to single cell activity

Running speed and pupil area are strongly correlated signals but do vary on different timescales (Figure 2 C-D) and have separable effects on neuronal activity (Vinck et al., 2015). Our analyses of ongoing spontaneous activity in AC and PPC also hint at the possibility of separable effects of pupil area and running speed, as AC Non-SOM neurons' activity was more highly correlated with pupil than with running speed ($p<0.0001$, paired permutation test).

To disentangle the relationships between neuronal activity, running velocity, and pupil area, we used an encoding model approach (Pillow et al., 2008; Park et al., 2014; Runyan et al., 2017). We constructed a Generalized Linear Model (GLM) that used sound stimulus timing and location, pupil area, and running velocity to predict the responses of individual SOM and Non-SOM neurons in AC and PPC, in the passive listening context (Figure 4A). It should be noted that in the above analyses (Figure 1 I, Figure 2

A-B, I), we considered only the speed at which the mouse was running in any direction, as increased running speed is correlated with heightened arousal (Fu et al., 2014; Zhou et al., 2014; McGinley et al., 2015; Vinck et al., 2015; Mineault et al., 2016; Shimaoka et al., 2018). Because PPC neurons' activity can be selective for running direction (Nitz, 2006; Whitlock et al., 2012; Runyan et al., 2017; Krumin et al., 2018; Minderer et al., 2019), in the GLM we used running velocity rather than speed to obtain more accurate predictions of each neuron's activity (Materials and Methods 7.0, Figure 4).

To determine the relative contributions of pupil area and running velocity to neurons' activity, we removed their predictors from the model and measured the decrement in the model's prediction performance. For example, we calculated the pupil size contribution to a given neuron's activity as the difference between the prediction performance of the model with and without the pupil size predictors. We considered this decrement in model performance as the contribution of pupil size to the neuron's activity (Materials and Methods 7.5). This approach allowed us to isolate the contributions of running velocity and pupil size that were not redundant with each other. If running velocity and pupil area did not make unique contributions to neuronal activity, running predictors would be able to account for the missing pupil area predictors and vice versa, and the performance of the model would not be degraded compared to the full model that includes both pupil area and running velocity predictors. The model comparison revealed single neuron activity that could be explained distinctly by running and by pupil in both AC and PPC (Figure 4 B-G, note neurons along the pupil and running contribution axes in D-G). While a Kruskal Wallis test indicated that the contribution of pupil size differed among the four cell-type/area combinations, post-hoc tests returned $p>.05$ for all pairwise comparisons (See Table 5 for full values and statistics). In contrast, running contributions were overall stronger in PPC neurons than in AC neurons ($p<0.0001$), and within PPC, running contributions were stronger to SOM than Non-SOM activity ($p<0.001$, Figure 4C, F, G). Within AC, running contributions did not depend on cell type ($p=0.44$, Figure 4C, D, E). See Table 5 for full values and statistics.

Sound location coding in AC and PPC

To characterize sound location specificity of responses in AC and PPC, we computed each neuron's sound location selectivity index (LSI) (Figure 5 A-D, Materials and Methods 9.0). Within both regions, Non-SOM neurons were more selective for sound location than SOM neurons ($p<0.0001$, Figure 5B-C). PPC neurons overall were less selective than AC neurons (Figure 5D), and PPC sound responses were less reliable than AC sound responses ($p<0.001$; Figure 5E). Based on these differences in sound location selectivity and response reliability, we expected population activity to represent sound location more accurately in AC than PPC.

To examine sound location coding at the level of populations, we built decoders to predict the most likely sound stimulus location (left vs right) using the activity of subsets of neurons. To compare the sound location coding by SOM neurons to the Non-SOM population, decoders used either SOM neurons or randomly subsampled (matched for n) Non-SOM neurons. We also selected an n-matched subset of the "best cells", single neurons with the best decoding in the same populations, for decoding. This allowed us to compare sound location decoding using the SOM and Non-SOM populations to the best possible decoding from the same overall local population. Each decoder was based on a Bayesian inversion of the encoding model (Figure 6A, Materials and Methods, 8.0; (Runyan et al., 2017)). The posterior probability of each stimulus was computed cumulatively at each timepoint using all previous timepoints in the trial. Decoder performance was quantified as the fraction of trials where the stimulus with the maximal posterior probability matched the actual presented stimulus.

First, to compare the overall ability of AC and PPC to represent sound location, we used activity of only the "best" cells (i.e., individual neurons whose activity best decoded sound location) regardless of cell type in the population decoder. The number of best cells used for each dataset was chosen to match the number of SOM neurons imaged during that session. The "best cell" decoder's performance was above chance when using activity from both AC and PPC (Figure 6 C-D, Materials and Methods, 8.0). However, as expected, AC decoding accuracy was greater than that of PPC ($p<0.0001$). Next, we compared the SOM and Non-SOM population decoders from each dataset. Within both areas, sound

location decoding was similar in SOM and Non-SOM populations (AC: $p=0.82$; PPC: $p=0.56$, unpaired permutation tests, Figure 6 C), and both cell type populations from AC outperformed decoding based on PPC populations ($p<0.0001$, unpaired permutation test, Figure 6 C-D). All cell-type specific, subsampled population decoders performed worse than the decoders based on the n-matched population of "best" neurons ($p<0.0001$, paired permutation test; Figure 6 D, See Materials and Methods 8.0). To summarize, sound location was better represented in AC than PPC, and SOM and random n-matched Non-SOM subpopulations in both areas were similarly informative about sound location. A sparse code for sound location was evident in both AC and PPC, as small numbers of highly tuned "best" neurons more accurately encoded sound location than the random subsamples of the population. See Table 6 for full values and statistics.

Sound location representations were enhanced with arousal in AC, but not PPC

Given the activity changes we observed in AC and PPC that accompanied increases in arousal, we hypothesized that arousal would affect sensory representations in both regions. To test this possibility, we tested decoders in low and high arousal periods. Sound stimulus trials were classified as occurring during low or high arousal based on the pupil size (Materials and Methods, 6.1, Figure 2 E), and low and high arousal trials were evenly balanced to train and test the decoders. Decoding performance for left vs. right sound location category using AC populations was modestly improved during heightened arousal ($p=0.0003$, paired permutation test), but decoding performance was similarly poor in low and high arousal trials using PPC populations (Figure 6 E-F) ($p=0.06$, paired permutation test). Thus, while sensory coding in AC was improved with heightened arousal, coding within PPC populations was unaffected by arousal state. See Table 6 for full values and statistics.

Discussion

We have measured spike-related activity in populations of somatostatin-expressing inhibitory interneurons (SOM) and Non-SOM neurons in auditory cortex (AC) and in posterior parietal cortex

(PPC), while mice experienced spontaneous shifts in arousal state. We examined the impact of these arousal state shifts on ongoing activity patterns, as well as on sound-evoked responses. In AC, the relationships between arousal and activity of individual neurons were diverse, with a slight net positive effect of heightened arousal on population activity. In PPC, activity of most neurons increased during heightened arousal states. In AC, SOM and Non-SOM populations were similarly heterogeneous in their arousal-related responses, while in PPC, SOM populations were even more strongly and uniformly activated with increased arousal than Non-SOM neurons.

Our results suggest that local circuits in AC, a sensory region of cortex, and PPC, an association-level region of cortex, have cell-type specific specializations that lead to distinct responses to changes in arousal state. The more prevalent negative modulation of activity during locomotion in AC could be the consequence of negative motor-related feedback from motor cortex through parvalbumin inhibitory interneurons in AC (Schneider et al., 2014; Zhou et al., 2014; Yavorska and Wehr, 2021). The overall positive modulation of SOM and Non-SOM neurons we observed in PPC is consistent with some descriptions of positive modulation of SOM and other neuron types in primary visual cortex (V1) in the presence of visual stimuli (Polack et al., 2013; Pakan et al., 2016), while others have described negative modulation of SOM neuron activity with locomotion in darkness (Fu et al., 2014). It is unclear whether the effects of locomotion in PPC will also vary with visual or other context changes. While similar local circuit motifs are present throughout cortex, differences in density and specificity of intrinsic connections or expression of neuromodulatory receptors could lead to specializations in the function of microcircuits as animals transition between behavioral states. Further work will be necessary to understand which specific local circuit specializations, particularly within SOM populations, relate to region-specific effects of arousal.

When mice increased their running speed, pupil size also increased (Figure 2A). Despite the strong correlation between these two behavioral correlates of arousal, we were able to disentangle the contributions of running velocity and pupil size to the activity of individual neurons in AC and PPC using

an encoding model (Figure 4). In both regions, pupil size and running velocity had unique, non-overlapping contributions to the activity of SOM and Non-SOM neurons. However, more of the arousal-related activity modulation in PPC was explained by changes in running velocity, while in AC, pupil size and running velocity were similarly weak contributors to activity. The strong running-related modulation of activity in PPC, particularly among SOM neurons, is likely related to its role in navigation and sensorimotor transformations (Andersen and Buneo, 2002; Harvey et al., 2012; Park et al., 2014; Goard et al., 2016; Licata et al., 2017; Runyan et al., 2017; Krumin et al., 2018).

The effects of arousal on neuronal activity and coding have been examined in depth across primary sensory cortices. In primary auditory cortex, the Yerkes-Dodson (inverted-U) relationship between pupil size and sound decoding has been observed (McGinley et al., 2015; Lin et al., 2019), which aligns well with the known links between norepinephrine levels and behavioral performance and an "optimal" level of arousal for behavioral performance (Waschke et al., 2019). We did not observe this effect, instead measuring a modest improvement in decoding accuracy with arousal. Mice in our experiments were most likely to visit two separable behavioral states (stationary/unaroused or running/aroused), without the gradation of different levels of arousal observed by others. Our "high" arousal state likely includes a mixture of the moderate and high arousal states defined by others when three separable states can be identified. It is important to note that while locomotion, whisking, and pupil dilations have all been considered as behavioral correlates of an animal's arousal state, motor-related feedback acts on specialized circuits within visual, somatosensory, and auditory cortices (Lee et al., 2013; Fu et al., 2014; Schneider et al., 2014; Pakan et al., 2016; Urban-Ciecko and Barth, 2016; Yavorska and Wehr, 2021) that interact with neuromodulatory inputs, leading to different arousal-related effects on network activity in those regions. It is unlikely that any aroused state is without a related change in fidgeting, facial movements, or other motor outputs (Musall et al., 2019; Stringer et al., 2019).

In contrast to AC, arousal state did not affect sensory representations in PPC, despite the more pronounced positive modulation of activity in PPC with increases in arousal (Figure 6). Previously, it has

been demonstrated that sensory coding in PPC depends on the behavioral relevance of a given stimulus in the context of a task (Fitzgerald et al., 2013; Pho et al., 2018). Task engagement is associated with more highly aroused states; however, in our results, arousal alone was not sufficient to improve sensory decoding in PPC outside of a task context. Our results support the idea that task engagement and arousal modulate sensory responses through separate pathways (Saderi et al., 2021). Here, we have isolated the global arousal state from the effects of task demands by measuring neuronal activity during spontaneous fluctuations in arousal and locomotion. In AC, but not PPC, sensory representations are enhanced with arousal, even when not behaviorally relevant. An important future direction will be to determine whether global shifts in arousal affect the coding of behaviorally relevant information in PPC.

Our results demonstrate that behavioral states have distinct effects on overall activity in AC, a primary sensory region, and in PPC, an association-level region of cortex. In PPC, where heightened arousal was associated with increased activity, SOM activity was more sensitive to changes in behavioral state than Non-SOM neuron activity. In AC, SOM and Non-SOM populations were more diversely modulated with arousal, with no apparent differences between cell types. Despite more the more subtle overall effects of arousal state on activity levels in AC, sensory representations were enhanced with heightened arousal in AC, but not PPC. Together, these findings imply specialization in the circuitry underlying state changes across the cortical hierarchy, particularly within the SOM subpopulation. These specializations likely support the unique functions of distinct regions in sensory representation in the case of AC or sensorimotor transformation in the case of PPC.

References

Adesnik H, Bruns W, Taniguchi H, Huang ZJ, Scanziani M (2012) A neuronal circuit for spatial summation in visual cortex. Nature 490:226–231.

Alitto HJ, Dan Y (2013) Cell-type-specific modulation of neocortical activity by basal forebrain input. Frontiers in Systems Neuroscience 6 Available at: https://www.frontiersin.org/articles/10.3389/fnsys.2012.00079/full.

Andersen RA, Buneo CA (2002) INTENTIONAL MAPS IN POSTERIOR PARIETAL CORTEX. Annu Rev Neurosci 25:189–220.

Beierlein M, Gibson JR, Connors BW (2000) A network of electrically coupled interneurons drives synchronized inhibition in neocortex. Nat Neurosci 3:904–910.

Bennett C, Arroyo S, Hestrin S (2013) Subthreshold Mechanisms Underlying State-Dependent Modulation of Visual Responses. Neuron 80:350–357.

Cantero JL, Atienza M, Salas RM, Gómez CM (1999) Brain Spatial Microstates of Human Spontaneous Alpha Activity in Relaxed Wakefulness, Drowsiness Period, and REM Sleep. Brain Topogr 11:257–263.

Chen N, Sugihara H, Sur M (2015) An acetylcholine-activated microcircuit drives temporal dynamics of cortical activity. Nature Neuroscience 18:892–902.

Chen T-W, Wardill TJ, Sun Y, Pulver SR, Renninger SL, Baohan A, Schreiter ER, Kerr RA, Orger MB, Jayaraman V, Looger LL, Svoboda K, Kim DS (2013) Ultrasensitive fluorescent proteins for imaging neuronal activity. Nature 499:295–300.

Cohen MR, Maunsell JHR (2009) Attention improves performance primarily by reducing interneuronal correlations. Nature Neuroscience 12:1594–1600.

Dienel SJ, Ciesielski AJ, Bazmi HH, Profozich EA, Fish KN, Lewis DA (2020) Distinct Laminar and Cellular Patterns of GABA Neuron Transcript Expression in Monkey Prefrontal and Visual Cortices. Cereb Cortex 31:bhaa341-.

Dipoppa M, Ranson A, Krumin M, Pachitariu M, Carandini M, Harris KD (2018) Vision and Locomotion Shape the Interactions between Neuron Types in Mouse Visual Cortex. Neuron 98:602-615.e8.

Elhilali M, Fritz JB, Klein DJ, Simon JZ, Shamma SA (2004) Dynamics of precise spike timing in primary auditory cortex. The Journal of neuroscience : the official journal of the Society for Neuroscience 24:1159–1172.

Fanselow EE, Richardson KA, Connors BW (2008) Selective, state-dependent activation of somatostatin-expressing inhibitory interneurons in mouse neocortex. Journal of neurophysiology 100:2640–2652 Available at: http://jn.physiology.org/cgi/content/full/100/5/2640.

Fino E, Yuste R (2011) Dense Inhibitory Connectivity in Neocortex. Neuron 69:1188–1203 Available at: http://dx.doi.org/10.1016/j.neuron.2011.02.025.

Fitzgerald JK, Freedman DJ, Fanini A, Bennur S, Gold JI, Assad JA (2013) Biased Associative Representations in Parietal Cortex. Neuron 77:180–191.

Friedman J, Hastie T, Tibshirani R (2010) Regularization Paths for Generalized Linear Models via Coordinate Descent. Journal of Statistical Software 33 Available at: https://www.jstatsoft.org/article/view/v033i01.

Friedrich J, Zhou P, Paninski L (2017) Fast online deconvolution of calcium imaging data. Plos Comput Biol 13:e1005423.

Fu Y, Tucciarone JM, Espinosa JS, Sheng N, Darcy DP, Nicoll RA, Huang ZJ, Stryker MP (2014) A Cortical Circuit for Gain Control by Behavioral State. Cell 156:1139–1152 Available at: https://www.sciencedirect.com/science/article/pii/S0092867414001445.

Garcia-Junco-Clemente P, Ikrar T, Tring E, Xu X, Ringach DL, Trachtenberg JT (2017) An inhibitory pull-push circuit in frontal cortex. Nat Neurosci 20:389–392.

Garcia-Junco-Clemente P, Tring E, Ringach DL, Trachtenberg JT (2019) State-Dependent Subnetworks of Parvalbumin-Expressing Interneurons in Neocortex. Cell Reports 26:2282-2288.e3.

Goard MJ, Pho GN, Woodson J, Sur M (2016) Distinct roles of visual, parietal, and frontal motor cortices in memory-guided sensorimotor decisions. eLife.

Gould IC, Rushworth MF, Nobre AC (2011) Indexing the graded allocation of visuospatial attention using anticipatory alpha oscillations. J Neurophysiol 105:1318–1326.

Grent-'t-Jong T, Boehler CN, Kenemans JL, Woldorff MG (2011) Differential functional roles of slow-wave and oscillatory-α activity in visual sensory cortex during anticipatory visual-spatial attention. Cereb Cortex New York N Y 1991 21:2204–2216.

Harvey CD, Coen P, Tank DW (2012) Choice-specific sequences in parietal cortex during a virtual-navigation decision task. Nature 484:62–68 Available at: http://www.nature.com/nature/journal/v484/n7392/abs/nature10918.html.

Karnani MM, Jackson J, Ayzenshtat I, Sichani AH, Manoocheri K, Kim S, Yuste R (2016) Opening Holes in the Blanket of Inhibition: Localized Lateral Disinhibition by VIP Interneurons. J Neurosci 36:3471–3480.

Kato HK, Gillet SN, Isaacson JS (2015) Flexible Sensory Representations in Auditory Cortex Driven by Behavioral Relevance. Neuron 88:1027–1039.

Kawaguchi Y, Shindou T (1998) Noradrenergic Excitation and Inhibition of GABAergic Cell Types in Rat Frontal Cortex. J Neurosci 18:6963–6976.

Khan AG, Poort J, Chadwick A, Blot A, Sahani M, Mrsic-Flogel TD, Hofer SB (2018) Distinct learning-induced changes in stimulus selectivity and interactions of GABAergic interneuron classes in visual cortex. Nature Neuroscience 21:851–859.

Kim Y, Yang GR, Pradhan K, Venkataraju KU, Bota M, Molino LCG del, Fitzgerald G, Ram K, He M, Levine JM, Mitra P, Huang ZJ, Wang X-J, Osten P (2017) Brain-wide Maps Reveal Stereotyped Cell-Type-Based Cortical Architecture and Subcortical Sexual Dimorphism. Cell 171:456-469.e22.

Krumin M, Lee JJ, Harris KD, Carandini M (2018) Decision and navigation in mouse parietal cortex. Elife 7:e42583.

Kuchibhotla KV, Gill JV, Lindsay GW, Papadoyannis ES, Field RE, Sten TAH, Miller KD, Froemke RC (2016) Parallel processing by cortical inhibition enables context-dependent behavior. Nature Neuroscience Available at: http://www.nature.com/neuro/journal/vaop/ncurrent/full/nn.4436.html.

Lee S, Kruglikov I, Huang ZJ, Fishell G, Rudy B (2013) A disinhibitory circuit mediates motor integration in the somatosensory cortex. Nature Neuroscience 16:1662–1670 Available at: https://www.nature.com/articles/nn.3544.

Licata AM, Kaufman MT, Raposo D, Ryan MB, Sheppard JP, Churchland AK (2017) Posterior Parietal Cortex Guides Visual Decisions in Rats. J Neurosci 37:4954–4966.

Lin P-A, Asinof SK, Edwards NJ, Isaacson JS (2019) Arousal regulates frequency tuning in primary auditory cortex. Proc National Acad Sci 116:25304–25310.

Livingstone MS, Hubel DH (1981) Effects of sleep and arousal on the processing of visual information in the cat. Nature 291:554–561.

Madisen L, Zwingman TA, Sunkin SM, Oh SW, Zariwala HA, Gu H, Ng LL, Palmiter RD, Hawrylycz MJ, Jones AR, Lein ES, Zeng H (2009) A robust and high-throughput Cre reporting and characterization system for the whole mouse brain. Nature Neuroscience 13:133–140 Available at: http://www.nature.com/neuro/journal/v13/n1/full/nn.2467.html.

Marrocco RT, Witte EA, Davidson MC (1994) Arousal systems. Curr Opin Neurobiol 4:166–170.

McAdams CJ, Maunsell JH (1999) Effects of attention on orientation-tuning functions of single neurons in macaque cortical area V4. J Neurosci Official J Soc Neurosci 19:431–441.

McGinley MJ, David SV, McCormick DA (2015) Cortical Membrane Potential Signature of Optimal States for Sensory Signal Detection. Neuron 87:179–192.

Minderer M, Brown KD, Harvey CD (2019) The Spatial Structure of Neuronal Encoding in Mouse Posterior Cortex during Navigation. Neuron.

Mineault PJ, Tring E, Trachtenberg JT, Ringach DL (2016) Enhanced Spatial Resolution During Locomotion and Heightened Attention in Mouse Primary Visual Cortex. The Journal of neuroscience : the official journal of the Society for Neuroscience 36:6382–6392 Available at: http://www.jneurosci.org/content/36/24/6382.short.

Mitchell JF, Sundberg KA, Reynolds JH (2009) Spatial Attention Decorrelates Intrinsic Activity Fluctuations in Macaque Area V4. Neuron 63:879–888.

Musall S, Kaufman MT, Juavinett AL, Gluf S, Churchland AK (2019) Single-trial neuronal dynamics are dominated by richly varied movements. Nat Neurosci 22:1677–1686.

Nakamura K (1999) Auditory spatial discriminatory and mnemonic neurons in rat posterior parietal cortex. Journal of neurophysiology 82:2503–2517.

Niell CM, Stryker MP (2010) Modulation of Visual Responses by Behavioral State in Mouse Visual Cortex. Neuron 65:472–479 Available at: https://www.sciencedirect.com/science/article/pii/S0896627310000590.

Nitz DA (2006) Tracking route progression in the posterior parietal cortex. Neuron 49:747–756 Available at: http://eutils.ncbi.nlm.nih.gov/entrez/eutils/elink.fcgi?dbfrom=pubmed&id=16504949&retmode=ref&cmd=prlinks.

Pachitariu M, Stringer C, Dipoppa M, Schröder S, Rossi LF, Dalgleish H, Carandini M, Harris KD (2017) Suite2p: beyond 10,000 neurons with standard two-photon microscopy. Biorxiv:061507.

Pakan JM, Lowe SC, Dylda E, Keemink SW, Currie SP, Coutts CA, Rochefort NL (2016) Behavioral-state modulation of inhibition is context-dependent and cell type specific in mouse visual cortex. Elife 5:e14985.

Park IM, Meister MLR, Huk AC, Pillow JW (2014) Encoding and decoding in parietal cortex during sensorimotor decision-making. Nature Neuroscience 17:1395–1403.

Pfeffer CK, Xue M, He M, Huang ZJ, Scanziani M (2013) Inhibition of Inhibition in Visual Cortex: The Logic of Connections Between Molecularly Distinct Interneurons. Nat Neurosci 16:1068–1076.

Pho GN, Goard MJ, Woodson J, Crawford B, Sur M (2018) Task-dependent representations of stimulus and choice in mouse parietal cortex. Nat Commun 9:2596.

Pi H-J, Hangya B, Kvitsiani D, Sanders JI, Huang ZJ, Kepecs A (2013) Cortical interneurons that specialize in disinhibitory control. Nature 503:521–524.

Pillow JW, Shlens J, Paninski L, Sher A, Litke AM, Chichilnisky EJ, Simoncelli EP (2008) Spatio-temporal correlations and visual signalling in a complete neuronal population. Nature 454:995–999 Available at: http://www.nature.com/doifinder/10.1038/nature07140.

Pinto L, Goard MJ, Estandian D, Xu M, Kwan AC, Lee S-H, Harrison TC, Feng G, Dan Y (2013) Fast modulation of visual perception by basal forebrain cholinergic neurons. Nat Neurosci 16:1857–1863.

Polack P-O, Friedman J, Golshani P (2013) Cellular mechanisms of brain state–dependent gain modulation in visual cortex. Nat Neurosci 16:1331–1339.

Poulet JFA, Petersen CCH (2008) Internal brain state regulates membrane potential synchrony in barrel cortex of behaving mice. Nature 454:881–885.

Rabinowitz NC, Goris RL, Cohen M, Simoncelli EP (2015) Attention stabilizes the shared gain of V4 populations. eLife 4:e08998.

Rikhye RV, Yildirim M, Hu M, Breton-Provencher V, Sur M (2021) Reliable sensory processing in mouse visual cortex through cooperative interactions between somatostatin and parvalbumin interneurons. J Neurosci:JN-RM-3176-20.

Runyan CA, Piasini E, Panzeri S, Harvey CD (2017) Distinct timescales of population coding across cortex. Nature 548:92–96 Available at: http://www.nature.com/nature/journal/v548/n7665/full/nature23020.html?foxtrotcallback=true.

Saderi D, Schwartz ZP, Heller CR, Pennington JR, David SV (2021) Dissociation of task engagement and arousal effects in auditory cortex and midbrain. Elife 10:e60153.

Schneider DM, Nelson A, Mooney R (2014) A synaptic and circuit basis for corollary discharge in the auditory cortex. Nature 513:189–194 Available at: http://www.nature.com/nature/journal/v513/n7517/full/nature13724.html.

Shimaoka D, Harris KD, Carandini M (2018) Effects of Arousal on Mouse Sensory Cortex Depend on Modality. Cell Reports 25:3230.

Stringer C, Pachitariu M, Steinmetz N, Reddy CB, Carandini M, Harris KD (2019) Spontaneous behaviors drive multidimensional, brainwide activity. Science 364:eaav7893.

Taniguchi H, He M, Wu P, Kim S, Paik R, Sugino K, Kvitsiani D, Kvitsani D, Fu Y, Lu J, Lin Y, Miyoshi G, Shima Y, Fishell G, Nelson SB, Huang ZJ (2011) A resource of Cre driver lines for genetic targeting of GABAergic neurons in cerebral cortex. Neuron 71:995–1013 Available at: http://dx.doi.org/10.1016/j.neuron.2011.07.026.

Tremblay R, Lee S, Rudy B (2016) GABAergic Interneurons in the Neocortex: From Cellular Properties to Circuits. Neuron 91:260–292 Available at: http://www.sciencedirect.com/science/article/pii/S0896627316303117.

Treue S, Maunsell JHR (1996) Attentional modulation of visual motion processing in cortical areas MT and MST. Nature 382:539–541 Available at: https://www.nature.com/articles/382539a0.

Urban-Ciecko J, Barth AL (2016) Somatostatin-expressing neurons in cortical networks. Nat Rev Neurosci 17:401–409.

Veit J, Hakim R, Jadi MP, Sejnowski TJ, Adesnik H (2017) Cortical gamma band synchronization through somatostatin interneurons. Nature Neuroscience 20:951–959.

Vinck M, Batista-Brito R, Knoblich U, Cardin JA (2015) Arousal and Locomotion Make Distinct Contributions to Cortical Activity Patterns and Visual Encoding. Neuron 86:740–754.

Wang X-J, Yang GR (2018) A disinhibitory circuit motif and flexible information routing in the brain. Curr Opin Neurobiol 49:75–83.

Waschke L, Tune S, Obleser J (2019) Local cortical desynchronization and pupil-linked arousal differentially shape brain states for optimal sensory performance. Elife 8:e51501.

Whitlock JR, Pfuhl G, Dagslott N, Moser M-B, Moser EI (2012) Functional split between parietal and entorhinal cortices in the rat. Neuron 73:789–802 Available at: http://eutils.ncbi.nlm.nih.gov/entrez/eutils/elink.fcgi?dbfrom=pubmed&id=22365551&retmode=ref&cmd=prlinks.

Wilson NR, Runyan CA, Wang FL, Sur M (2012) Division and subtraction by distinct cortical inhibitory networks in vivo. Nature 488:343–348 Available at: http://eutils.ncbi.nlm.nih.gov/entrez/eutils/elink.fcgi?dbfrom=pubmed&id=22878717&retmode=ref&cmd=prlinks.

Xiang Z, Huguenard JR, Prince DA (1998) Cholinergic switching within neocortical inhibitory networks. Science 281:985–988 Available at: http://www.sciencemag.org/cgi/content/full/281/5379/985.

Xu H, Jeong H-Y, Tremblay R, Rudy B (2013) Neocortical Somatostatin-Expressing GABAergic Interneurons Disinhibit the Thalamorecipient Layer 4. Neuron 77:155–167 Available at: http://www.sciencedirect.com/science/article/pii/S0896627312009956#.

Yavorska I, Wehr M (2021) Effects of Locomotion in Auditory Cortex Are Not Mediated by the VIP Network. Front Neuronal Circuit 15:618881.

Zhou M, Liang F, Xiong XR, Li L, Li H, Xiao Z, Tao HW, Zhang LI (2014) Scaling down of balanced excitation and inhibition by active behavioral states in auditory cortex. Nature Neuroscience 17:841–850.

Figure Legends

Figure 1: Imaging spike-related activity in SOM and Non-SOM neurons during behavioral state transitions. (A) Viral injections and cranial windows were made over auditory cortex (AC) and posterior parietal cortex (PPC) in each SOM-tdTomato mouse. (B) In imaging sessions, mice were headfixed over a spherical treadmill and allowed to run voluntarily. Four speakers arranged around the head presented sound stimuli. An infrared camera was used to image the pupil, and a rotating two-photon microscope was focused on either AC or PPC on a given imaging day. (C) Each imaging session included "Spontaneous" and "Passive Listening" contexts, without or with randomly presented sound stimuli from each of eight locations, respectively. (D) Pupil area was monitored via the pupil camera, scalebar in bottom image applies to top (constricted pupil) and bottom (dilated pupil). (E) Example field of view from auditory cortex, with intermingled tdTomato+/SOM+ (magenta) and tdTomato-/SOM- neurons, co-expressing GCaMP6f (green). (F) Example aligned behavioral and neural signals collected during the imaging session in E, including running speed (cm/s), normalized pupil area, dF/F from a Non-SOM (red) and SOM neuron (orange), each overlaid with the neuron's deconvolved estimated spike rates. (G) As in

E, for an example posterior parietal cortex field of view. (H) As in F, for the PPC field of view in G. (I) Proportions of Non-SOM and SOM neurons in AC (left) and PPC (right) with significant positive (white), negative (black), or no modulation by mouse's running onset. AC Non-SOM N=2645; AC SOM N=359; PPC Non-SOM N=4719; PPC SOM N=525. (J) As in I, for pupil dilation. (K) Proportion of Non-SOM and SOM neurons in AC and PPC that were significantly sound responsive to at least one location (white) or not significantly sound responsive (black).

Figure 2: Single cell activity modulation with increases in arousal. (A) Average z-scored deconvolved activity, running speed, and pupil area aligned on running bout onset. Red: AC Non-SOM neurons' activity (N=24 datasets), Orange: AC SOM neurons' activity (N=24 datasets), Dark Blue: PPC Non-SOM neurons' activity (N=20 datasets), Light Blue: PPC SOM neurons' activity (N=20 datasets), Black: Running speed (N=44 datasets), Gray: Pupil area (N=44 datasets). (B) Average z-scored deconvolved activity of individual neurons, from L to R: all AC Non-SOM, AC SOM, PPC Non-SOM, and PPC SOM neurons aligned on running bout onset (AC Non-SOM N=2645; AC SOM N=359; PPC Non-SOM N=4719; PPC SOM N=525, in B-I). Neurons were sorted by running modulation. (C) Autocorrelation of pupil area and running speed, averaged across all datasets (N=44). (D) Crosscorrelation between running speed and pupil area, averaged across all datasets (N=44). Black triangle indicates time lag with peak correlation, with runing preceding pupil by 1.27 s. (E) Illustration of clustering that sorted pupil area during each imaging frame into low, transition, and high arousal states. (F) Mean responses of AC Non-SOM (red solid), AC SOM (red dotted), PPC Non-SOM (blue solid), and PPC SOM (blue dotted) neurons in low and high arousal states, as defined in E. (G) Left: Mean activity of AC Non-SOM neurons in high arousal state (classified with clustering as in C), plotted against mean activity in the low arousal state. Right: Mean activity of AC SOM neurons in high arousal vs low arousal states. (H) As in E, for PPC Non-SOM and SOM neurons. (I) Cumulative probability distribution of the arousal modulation index in AC Non-SOM (solid red), AC SOM (dotted red), PPC Non-SOM (solid blue), and PPC SOM (dotted blue) neurons. Arousal modulation index was calculated from the values in E-F, (High-

Low)/(High+Low) for each neuron. (J) Cumulative probability distribution of the Pearson correlation between each neuron's activity and pupil area, colors as in G. (K) Cumulative probability distribution of the Pearson correlation between each neuron's activity and running speed. Significance as indicated, permutation test, **** p<.0001. Error bars: 95% bootstrapped confidence interval around the mean.

Figure 3: Single cell activity relationships with pupil area and running speed, in the passive listening context. Analyses are the same as presented in Figure 2E-K, but in the passive listening context. AC Non-SOM N=2645; AC SOM N=359; PPC Non-SOM N=4719; PPC SOM N=525 for all panels. (A) Schematic showing passive listening context. (B) Mean responses of AC Non-SOM (red solid), AC SOM (red dotted), PPC Non-SOM (blue solid), and PPC SOM (blue dotted) neurons in low and high arousal states, as defined in A. ****p<.0001, lines represent bootstrapped 95% confidence intervals. (C) Left: Mean activity of AC Non-SOM neurons in high arousal state (classified with clustering as in A), plotted against mean activity in the low arousal state. Right: Mean activity of AC SOM neurons in high arousal vs low arousal states. (D) As in C, for PPC Non-SOM and SOM neurons. (E) Cumulative probability distribution of the arousal modulation index in AC Non-SOM (solid red), AC SOM (dotted red), PPC Non-SOM (solid blue), and PPC SOM (dotted blue) neurons. Arousal modulation index was calculated from the values in C-D, (High-Low)/(High+Low) for each neuron. (F) Cumulative probability distribution of the Pearson correlation between each neuron's activity and pupil area, colors as in E. (G) Cumulative probability distribution of the Pearson correlation between each neuron's activity and running speed.

Figure 4: Using an Encoding Model to Disentange Running and Pupil Contributions to Single Cell Activity. (A) Schematic of Generalized Linear Model (GLM) used to determine contributions of pupil area and running velocity to neurons' activity. (B) Average contribution of pupil area to activity across all AC Non-SOM (N=2645) and SOM (N=359) neurons (red bars) and PPC Non-SOM (N=4525) and SOM (N=505) neurons (blue bars). Contribution was quantified as the improvement in model prediction performance of each neuron's activity when adding pupil area as a set of predictors. Errorbars indicate

SEM, n.s., not significant, exact values in text. (C) As in B, calculated when comparing model performance with and without running velocity predictors. AC Non-SOM and SOM neurons (red bars) and PPC Non-SOM and SOM neurons (blue bars), ****p<.0001. (D) Pupil contribution plotted against running contribution for each AC Non-SOM neuron, calculated as in B. (E) Pupil contribution plotted against running contribution for each AC SOM neuron. (F-G) Pupil contribution plotted against running contribution for each PPC Non-SOM or SOM neuron. Sample sizes in B apply to all panels.

Figure 5: Sound Location Selectivity in AC and PPC. (A) Six example neurons with diverse sound location preferences, ranging from ipsilateral (-90 - 0 degrees) to contralateral locations (0 - +90 degrees). Thin lines: mean response during sound presentation of individual trials. Thick lines: Trial average. The location selectivity index (LSI) and response reliability are reported for each example cell. Red: Example Non-SOM neurons. Orange: Example SOM neuron. (B) Distribution of Location Selectivity Index (LSI) for Non-SOM (0.20 [0.20, 0.21] , N=2455) and SOM (.19 [0.18, .19], N=354) neurons in AC. Triangles indicate population means. (C) As in B, for PPC Non-SOM (0.20 [0.19, 0.20], N=2553) and SOM (.13 [.12, .14], N=298). (D) Mean location selectivity index in AC and PPC. (E) Cumulative distributions of response reliability, the fraction of sound-responsive trials, in AC and PPC. * p<0.05, ***p<0.001, ****p<0.0001, error bars indicate SEM.

Figure 6: Decoding Sound Location from AC and PPC Population Activity. (A) The encoding model was trained on all trials that included all arousal levels, and inverted using Bayes Rule to compute the posterior probability of auditory stimuli given the activity of the neural population in AC and PPC . (B) Schematic of the discrimination being performed by the decoder, classifying sound stimuli as occuring from the left or right of the mouse. (C) Left: Mean cumulative population decoder performance (across datasets) when classifying left vs right locations, when based on “best cells”, defined as individual Non-SOM cells or SOM cells with the highest decoding performance. “Best cells” and Non-SOM cells in each dataset were subsampled to match the N of the SOM neuron population within each imaging field of view. Right: Population decoder performance using PPC neurons. Chance performance is 0.5. (D) Mean

decoder performance using all timepoints in the trial (equivalent to the final timepoints in (C) using SOM neurons, subsampled Non-SOM neurons, and "best cells" in AC and PPC. Dotted line corresponds to chance performance (50%). (E) Mean fraction correct of cumulative sound location (left sound locations vs right sound locations) decoding in AC (right) and PPC (left) populations in high (dark) and low (light) arousal conditions. Subsampling to match arousal and sound locations was repeated 10x. (F) Cumulative fraction correct of decoding for left vs right sound location at the end of the trial in AC and PPC. Shading in C,E and errorbars in D,F indicate SEM, **** $p<0.0001$, n.s. not significant. AC Non-SOM N=24 datasets; AC SOM N=24 datasets; PPC Non-SOM N=20 datasets; PPC SOM N=20 datasets throughout figure panels.

Table Titles/Legends

Table 1: Arousal Modulation Index during spontaneous context/Full values and statistics related to Figure 2I

Table 2: Correlation coefficients with pupil area and running speed during spontaneous context/Full values and statistics related to Figure 2J-K

Table 3: Arousal Modulation Index during passive listening context/Full values and statistics related to Figure 3E

Table 4: Correlation coefficients with pupil area and running speed during passive listening context/Full values and statistics related to Figure 3F-G

Table 5: Pupil and Running Contributions/Full values and statistics related to Figure 4

Table 6: Sound Location Decoding/Full values and statistics related to Figure 6

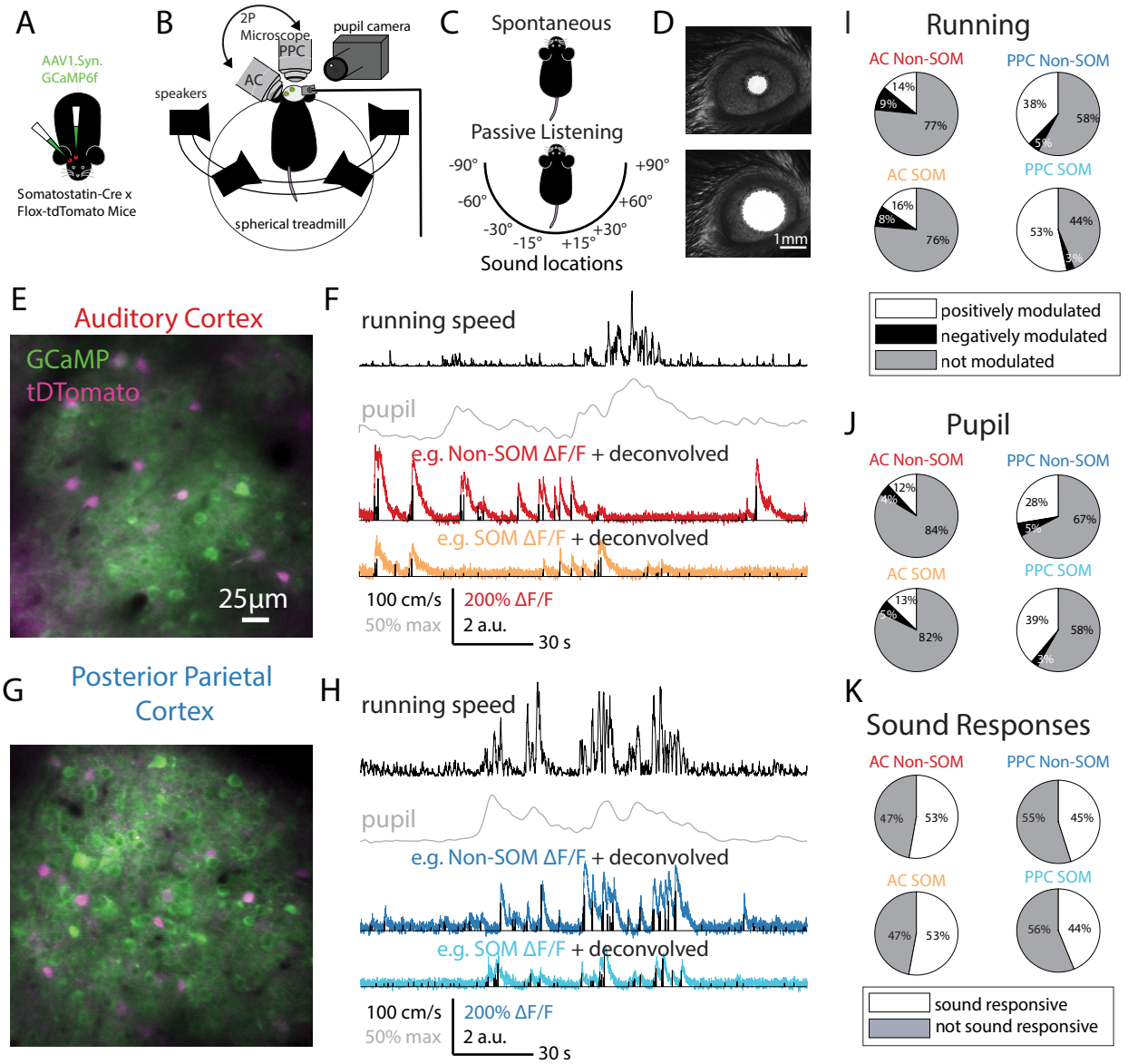

Figure 1: Imaging spike-related activity in SOM and Non-SOM neurons during behavioral state transitions. (A) Viral injections and cranial windows were made over auditory cortex (AC) and posterior parietal cortex (PPC) in each SOM-tdTomato mouse. (B) In imaging sessions, mice were headfixed over a spherical treadmill and allowed to run voluntarily. Four speakers arranged around the head presented sound stimuli. An infrared camera was used to image the pupil, and a rotating two-photon microscope was focused on either AC or PPC on a given imaging day. (C) Each imaging session included "Spontaneous" and "Passive Listening" contexts, without or with randomly presented sound stimuli from each of eight locations, respectively. (D) Pupil area was monitored via the pupil camera, scalebar in bottom image applies to top (constricted pupil) and bottom (dilated pupil). (E) Example field of view from auditory cortex, with intermingled tdTomato+/SOM+ (magenta) and tdTomato-/SOM- neurons, co-expressing GCaMP6f (green). (F) Example aligned behavioral and neural signals collected during the imaging session in E, including running speed (cm/s), normalized pupil area, dF/F from a Non-SOM (red) and SOM neuron (orange), each overlaid with the neuron's deconvolved estimated spike rates. (G) As in E, for an example posterior parietal cortex field of view. (H) As in F, for the PPC field of view in G. (I) Proportions of Non-SOM and SOM neurons in AC (left) and PPC (right) with significant positive (white), negative (black), or no modulation by mouse's running onset. AC Non-SOM N=2645; AC SOM N=359; PPC Non-SOM N=4719; PPC SOM N=525. (J) As in I, for pupil dilation. (K) Proportion of Non-SOM and SOM neurons in AC and PPC that were significantly sound responsive to at least one location (white) or not significantly sound responsive (black).

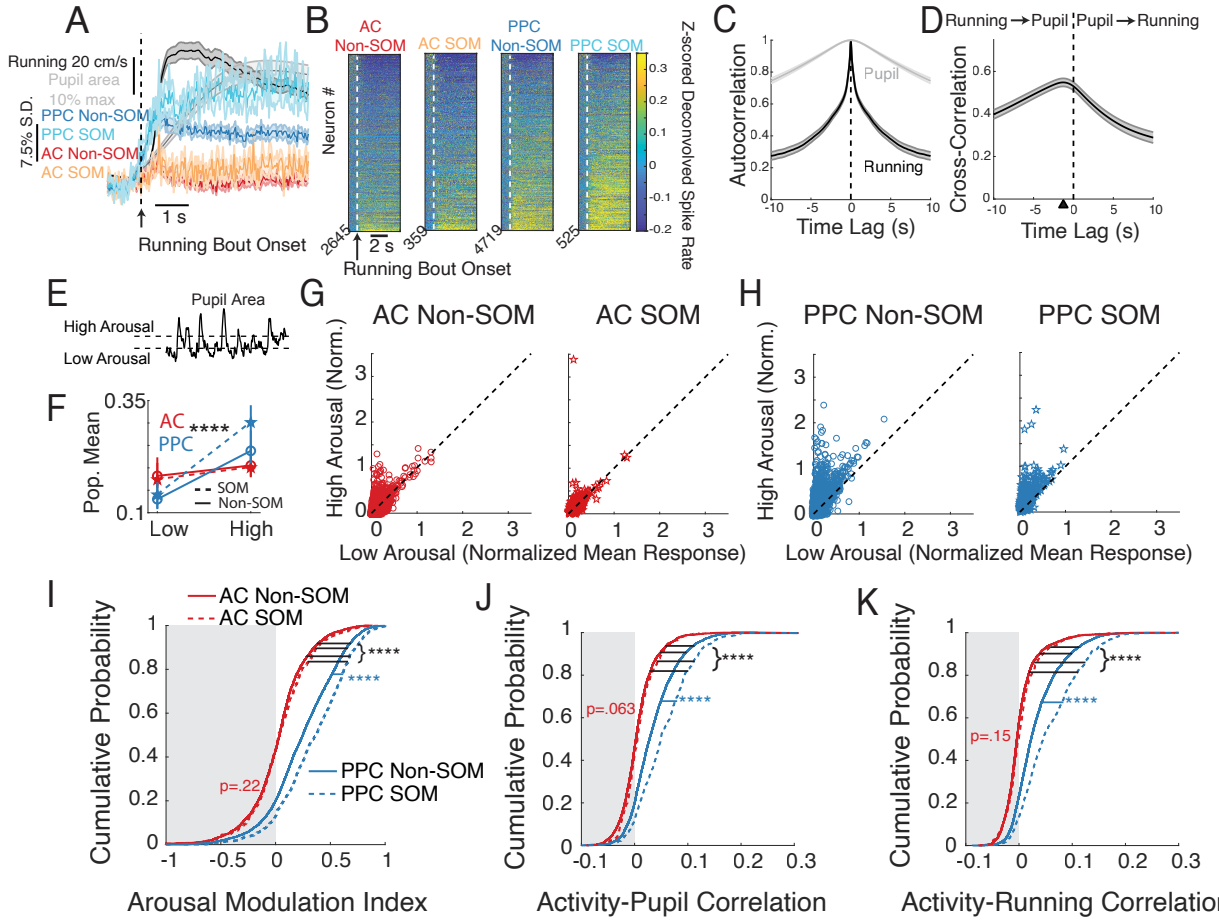

Figure 2: Single cell activity modulation with increases in arousal. (A) Average z-scored deconvolved activity, running speed, and pupil area aligned on running bout onset. Red: AC Non-SOM neurons' activity (N=24 datasets), Orange: AC SOM neurons' activity (N=24 datasets), Dark Blue: PPC Non-SOM neurons' activity (N=20 datasets), Light Blue: PPC SOM neurons' activity (N=20 datasets), Black: Running speed (N=44 datasets), Gray: Pupil area (N=44 datasets). (B) Average z-scored deconvolved activity of individual neurons, from L to R: all AC Non-SOM, AC SOM, PPC Non-SOM, and PPC SOM neurons aligned on running bout onset (AC Non-SOM N=2645; AC SOM N=359; PPC Non-SOM N=4719; PPC SOM N=525, in B-I). Neurons were sorted by running modulation. (C) Autocorrelation of pupil area and running speed, averaged across all datasets (N=44). (D) Crosscorrelation between running speed and pupil area, averaged across all datasets (N=44). Black triangle indicates time lag with peak correlation, with runing preceding pupil by 1.27 s. (E) Illustration of clustering that sorted pupil area during each imaging frame into low, transition, and high arousal states. (F) Mean responses of AC Non-SOM (red solid), AC SOM (red dotted), PPC Non-SOM (blue solid), and PPC SOM (blue dotted) neurons in low and high arousal states, as defined in E. (G) Left: Mean activity of AC Non-SOM neurons in high arousal state (classified with clustering as in C), plotted against mean activity in the low arousal state. Right: Mean activity of AC SOM neurons in high arousal vs low arousal states. (H) As in E, for PPC Non-SOM and SOM neurons. (I) Cumulative probability distribution of the arousal modulation index in AC Non-SOM (solid red), AC SOM (dotted red), PPC Non-SOM (solid blue), and PPC SOM (dotted blue) neurons. Arousal modulation index was calculated from the values in E-F, (High-Low)/(High+Low) for each neuron. (J) Cumulative probability distribution of the Pearson correlation between each neuron's activity and pupil area, colors as in G. (K) Cumulative probability distribution of the Pearson correlation between each neuron's activity and running speed. Significance as indicated, permutation test, **** p<.0001. Error bars: 95% bootstrapped confidence interval around the mean.

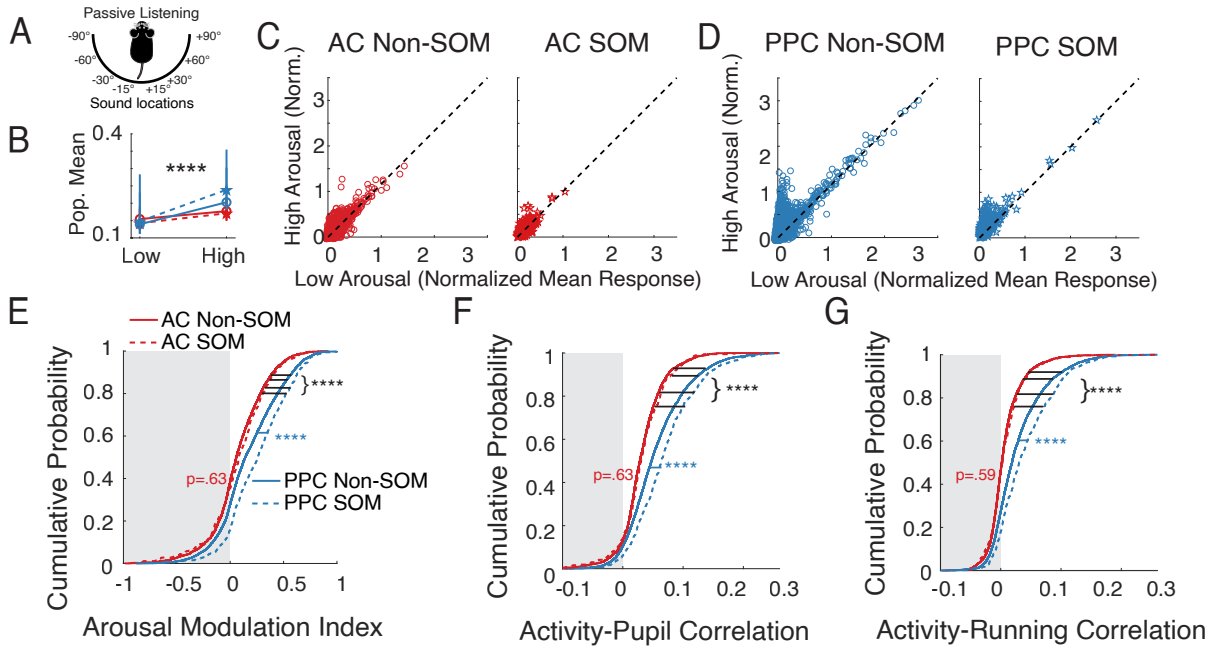

Figure 3: Single cell activity relationships with pupil area and running speed, in the passive listening context. Analyses are the same as presented in Figure 2E-K, but in the passive listening context. AC Non-SOM N=2645; AC SOM N=359; PPC Non-SOM N=4719; PPC SOM N=525 for all panels. (A) Schematic showing passive listening context. (B) Mean responses of AC Non-SOM (red solid), AC SOM (red dotted), PPC Non-SOM (blue solid), and PPC SOM (blue dotted) neurons in low and high arousal states, as defined in A. ****p<.0001, lines represent bootstrapped 95% confidence intervals. (C) Left: Mean activity of AC Non-SOM neurons in high arousal state (classified with clustering as in A), plotted against mean activity in the low arousal state. Right: Mean activity of AC SOM neurons in high arousal vs low arousal states. (D) As in C, for PPC Non-SOM and SOM neurons. (E) Cumulative probability distribution of the arousal modulation index in AC Non-SOM (solid red), AC SOM (dotted red), PPC Non-SOM (solid blue), and PPC SOM (dotted blue) neurons. Arousal modulation index was calculated from the values in C-D, (High-Low)/(High+Low) for each neuron. (F) Cumulative probability distribution of the Pearson correlation between each neuron's activity and pupil area, colors as in E. (G) Cumulative probability distribution of the Pearson correlation between each neuron's activity and running speed.

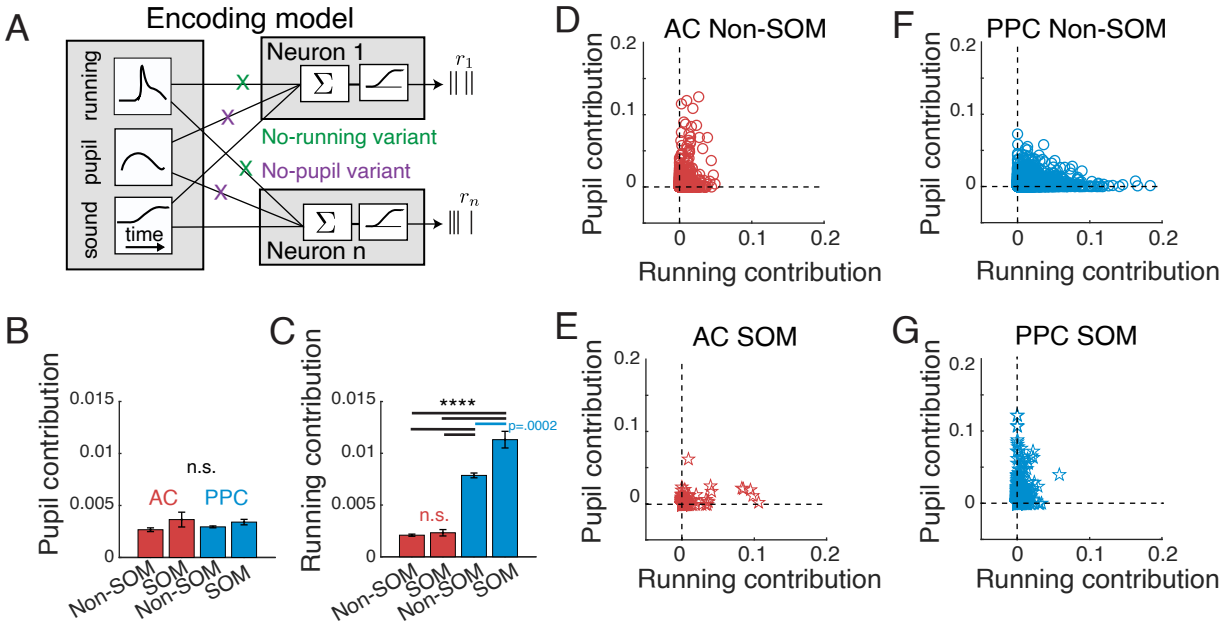

Figure 4: Using an Encoding Model to Disentange Running and Pupil Contributions to Single Cell Activity. (A) Schematic of Generalized Linear Model (GLM) used to determine contributions of pupil area and running velocity to neurons' activity. (B) Average contribution of pupil area to activity across all AC Non-SOM (N=2645) and SOM (N=359) neurons (red bars) and PPC Non-SOM (N=4525) and SOM (N=505) neurons (blue bars). Contribution was quantified as the improvement in model prediction performance of each neuron's activity when adding pupil area as a set of predictors. Errorbars indicate SEM, n.s., not significant, exact values in text. (C) As in B, calculated when comparing model performance with and without running velocity predictors. AC Non-SOM and SOM neurons (red bars) and PPC Non-SOM and SOM neurons (blue bars), ****p<.0001. (D) Pupil contribution plotted against running contribution for each AC Non-SOM neuron, calculated as in B. (E) Pupil contribution plotted against running contribution for each AC SOM neuron. (F-G) Pupil contribution plotted against running contribution for each PPC Non-SOM or SOM neuron. Sample sizes in B apply to all panels.

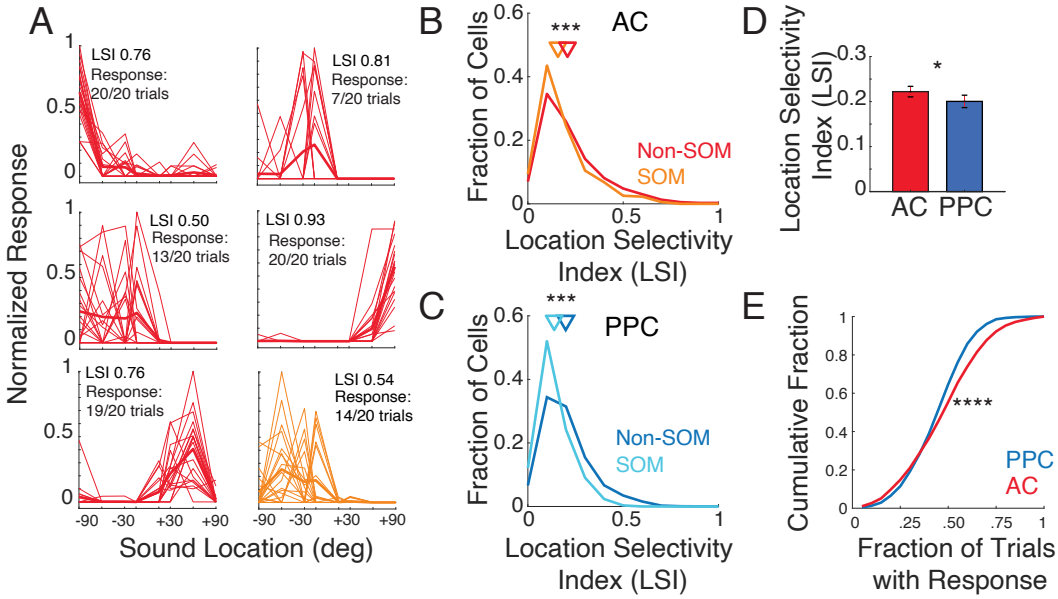

Figure 5: Sound Location Selectivity in AC and PPC. (A) Six example neurons with diverse sound location preferences, ranging from ipsilateral (-90 - 0 degrees) to contralateral locations (0 - +90 degrees). Thin lines: mean response during sound presentation of individual trials. Thick lines: Trial average. The location selectivity index (LSI) and response reliability are reported for each example cell. Red: Example Non-SOM neurons. Orange: Example SOM neuron. (B) Distribution of Location Selectivity Index (LSI) for Non-SOM (0.20 [0.20, 0.21] , N=2455) and SOM (.19 [0.18, .19], N=354) neurons in AC. Triangles indicate population means. (C) As in B, for PPC Non-SOM (0.20 [0.19, 0.20], N=2553) and SOM (.13 [.12, .14], N=298). (D) Mean location selectivity index in AC and PPC. (E) Cumulative distributions of response reliability, the fraction of sound-responsive trials, in AC and PPC. * $p<0.05$, ***$p<0.001$, ****$p<0.0001$, error bars indicate SEM.

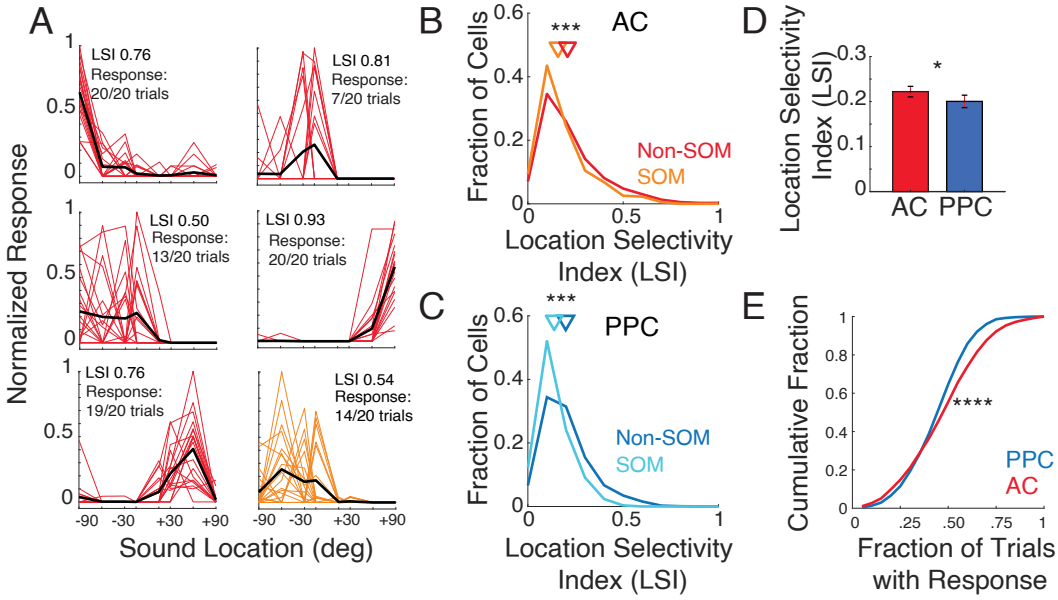

Figure 5: Sound Location Selectivity in AC and PPC. (A) Six example neurons with diverse sound location preferences, ranging from ipsilateral (-90 - 0 degrees) to contralateral locations (0 - +90 degrees). Thin lines: mean response during sound presentation of individual trials. Thick lines: Trial average. The location selectivity index (LSI) and response reliability are reported for each example cell. Red: Example Non-SOM neurons. Orange: Example SOM neuron. (B) Distribution of Location Selectivity Index (LSI) for Non-SOM (0.20 [0.20, 0.21] , N=2455) and SOM (.19 [0.18, .19], N=354) neurons in AC. Triangles indicate population means. (C) As in B, for PPC Non-SOM (0.20 [0.19, 0.20], N=2553) and SOM (.13 [.12, .14], N=298). (D) Mean location selectivity index in AC and PPC. (E) Cumulative distributions of response reliability, the fraction of sound-responsive trials, in AC and PPC. * $p<0.05$, ***$p<0.001$, ****$p<0.0001$, error bars indicate SEM.

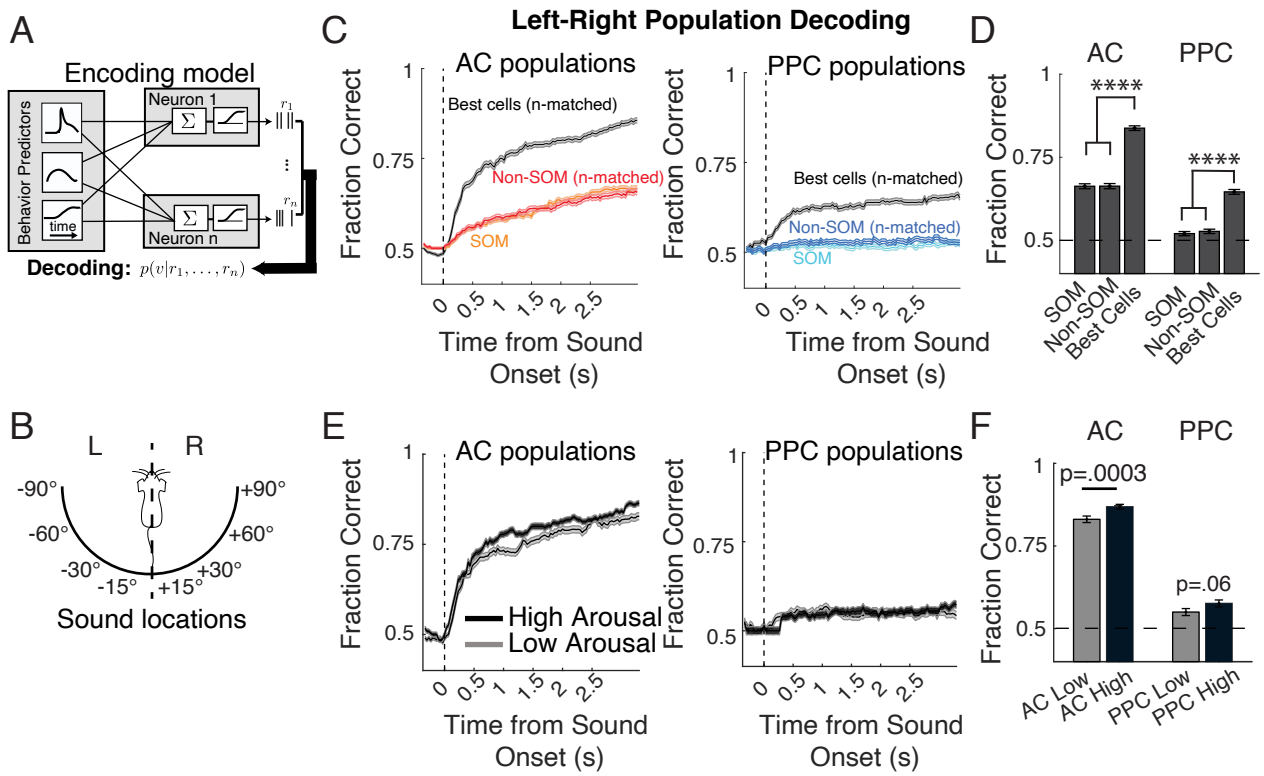

Figure 6: Decoding Sound Location from AC and PPC Population Activity. (A) The encoding model was trained on all trials that included all arousal levels, and inverted using Bayes Rule to compute the posterior probability of auditory stimuli given the activity of the neural population in AC and PPC . (B) Schematic of the discrimination being performed by the decoder, classifying sound stimuli as occuring from the left or right of the mouse. (C) Left: Mean cumulative population decoder performance (across datasets) when classifying left vs right locations, when based on "best cells", defined as individual Non-SOM cells or SOM cells with the highest decoding performance. "Best cells" and Non-SOM cells in each dataset were subsampled to match the N of the SOM neuron population within each imaging field of view. Right: Population decoder performance using PPC neurons. Chance performance is 0.5. (D) Mean decoder performance using all timepoints in the trial (equivalent to the final timepoints in (C) using SOM neurons, subsampled Non-SOM neurons, and "best cells" in AC and PPC. Dotted line corresponds to chance performance (50%). (E) Mean fraction correct of cumulative sound location (left sound locations vs right sound locations) decoding in AC (right) and PPC (left) populations in high (dark) and low (light) arousal conditions. Subsampling to match arousal and sound locations was repeated 10x. (F) Cumulative fraction correct of decoding for left vs right sound location at the end of the trial in AC and PPC. Shading in C,E and errorbars in D,F indicate SEM, **** p<0.0001, n.s. not significant. AC Non-SOM N=24 datasets; AC SOM N=24 datasets; PPC Non-SOM N=20 datasets; PPC SOM N=20 datasets throughout figure panels.